



## Article

# Soil and Rockfill Dams Safety Assessment for Henan Province: Monitoring, Analysis and Prediction

Hui Liu <sup>1,\*</sup>, Mengyuan Zhu <sup>1</sup>, Wu Zhu <sup>2</sup>, Wenfei Zhao <sup>1,3</sup>, Zechao Bai <sup>4</sup>, Bochen Zhou <sup>1</sup>, Geshuang Li <sup>5</sup> and Yuanxi Wang <sup>6</sup>

<sup>1</sup> College of Surveying and Geo-Informatics, North China University of Water Resources and Electric Power, Zhengzhou 450046, China

<sup>2</sup> College of Geological Engineering and Geomatics, Chang'an University, Xi'an 710054, China

<sup>3</sup> Hebei Institute of Investigation & Design of Water Conservancy & Hydropower Group Co., Ltd., Tianjin 300202, China

<sup>4</sup> School of Electrical and Control Engineering, North China University of Technology, Beijing 100144, China

<sup>5</sup> Department of Space Information Engineering, Henan College of Surveying and Mapping, Zhengzhou 450015, China

<sup>6</sup> College of Professional Study, Northeastern University, Boston, MA 02115, USA

\* Correspondence: liuhui\_celui@ncwu.edu.cn; Tel.: +86-18530079962

**Abstract:** It is of great significance to explore the spatial and temporal evolution of soil and rockfill dam deformation, ensuring the safety of people's lives and healthy economic development. The spatial and temporal evolution patterns of deformation of 17 large soil and rockfill dams in Henan Province were analyzed by using the PS-InSAR technique and 55 Sentinel-1A images from March 2017 to September 2021. Based on factors such as reservoir water level and rainfall, a series of analyses were conducted on the Xiaolangdi soil and rockfill dam, which has the highest dam height and the most prominent deformation problem. The monitoring results show that all the soil and rockfill dams in Henan Province have different degrees of deformation, and there is a close relationship between dam height and deformation. In addition, the deformation rate of the Xiaolangdi soil and rockfill dam in the past five years presents a "Stepped Shape" deformation trend from the top to the bottom of the dam. The deformation of the upper, middle, and lower parts of the dam body reaches 80 mm, 40 mm, and 20 mm, respectively, among which the middle part of the dam crest has the largest deformation. Furthermore, the time series prediction model for sparrow search algorithm Long Short-Term Memory considering the moving average filter (MAF-SSA-LSTM) is proposed to predict and accurately analyze the future deformation of Xiaolangdi soil and rockfill dam with RMSE of 1.526 mm, MAE of 1.447 mm, and MAPE of 2.22%, which proved that the model has high prediction accuracy. It can truly reflect the overall deformation trend of the dam body. The results provide a theoretical basis and decision basis for the census of reservoir safety conditions and deformation history retrieval in Henan Province.

**Keywords:** PS-InSAR; soil and rockfill dam; deformation monitoring; MAF-SSA-LSTM neural network



**Citation:** Liu, H.; Zhu, M.; Zhu, W.; Zhao, W.; Bai, Z.; Zhou, B.; Li, G.; Wang, Y. Soil and Rockfill Dams Safety Assessment for Henan Province: Monitoring, Analysis and Prediction. *Remote Sens.* **2023**, *15*, 4293. <https://doi.org/10.3390/rs15174293>

Academic Editors: Roberto Tomás, Joaquim João Sousa, Antonio Miguel Ruiz Armenteros and M. Clara de Lacy

Received: 17 July 2023

Revised: 22 August 2023

Accepted: 29 August 2023

Published: 31 August 2023



**Copyright:** © 2023 by the authors. Licensee MDPI, Basel, Switzerland. This article is an open access article distributed under the terms and conditions of the Creative Commons Attribution (CC BY) license (<https://creativecommons.org/licenses/by/4.0/>).

## 1. Introduction

China is the most developed country in the world in terms of large-scale water conservancy facilities. By the end of 2022, China had more than 98,000 reservoir dams, and Henan Province had 2538 reservoir dams, of which 48% were built in the 1950s–1970s, and 93% were soil and rockfill dams that had been in use for over 50 years. A large number of water conservancy projects are in "Extended Service" and "Exceeding Service", and the risk of failure cannot be fully controlled [1,2]. Restricted by the technical conditions of the 1950s, soil and rockfill dams were often surveyed, designed, and constructed at the same time, resulting in many dangerous reservoirs. Between 1954 and 1971, a total of 159 dam failure accidents occurred in Henan Province, with a dam failure rate of 6.27%, which was at a

relatively high level nationwide during the same period [3]. Especially in the flood season, for small- and medium-sized reservoir dams, river embankment failure and other hidden dangers, if not “belt and braces”, maybe “a failure of all”.

Traditional water conservancy project safety monitoring is mainly based on precision leveling measurements, Global Navigation Satellite System (GNSS) measurements, and sensors installed in the project. These low spatial sampling density methods can only obtain local point deformation, making it difficult to analyze the impact on the dam by combining factors such as reservoir water level and rainfall. At the same time, it will lead to an increase in the cost of human and material resources. The first two methods of measuring personnel need to enter the deformation area, increasing the risk; the latter method of the sensor is difficult to maintain and will gradually lose sensitivity and even effectiveness with the operation of the dam. Interferometric Synthetic Aperture Radar (InSAR) technique with surface-domain deformation monitoring capability can provide a more effective method for water resources engineering safety monitoring [4–8]. This method can effectively overcome the disadvantages of traditional monitoring, such as high maintenance cost, small monitoring range, low efficiency, and difficulty in predicting deformation. It has been widely used in monitoring geological hazards such as urban surface deformation [9–11], mountain landslides [12–14], mine deformation [15–18], earthquakes [19–21] and glacial permafrost [22–25].

Although the InSAR technique started relatively late, it has developed rapidly in the field of water conservancy engineering safety monitoring. This technique improves the accuracy and safety of dam deformation monitoring by providing high-resolution images to obtain accurate deformation information and has been validated in multiple studies [26–28]. As early as 2009, researchers began to explore the application of the InSAR technique in the stability monitoring of water conservancy buildings. Some typical cases include the application of the InSAR technique in the deformation monitoring and simulation model construction of the Three Gorges Dam [14,29,30], the application of reservoir dam deformation monitoring [31–33], and the application of the Persistent Scatterer Interferometric Synthetic Aperture Radar (PS-InSAR) technique in the reservoir landslide monitoring [34–36]. With the continuous progress and development of the InSAR technique, a series of studies have been carried out in recent years on dam slope deformation monitoring by combining the InSAR technique with groundwater level and temperature variations [37–39]. Therefore, the InSAR technique has played an active role in improving the efficiency of reservoir dam deformation monitoring and protecting the safe operation of water conservancy projects [40,41]. However, there is no overall analysis of the field of soil and rockfill dams, and there is a lack of attention to the particularity of soil and rockfill dam structures.

This study utilizes the PS-InSAR technique to monitor 17 large-scale soil and rockfill dams in Henan Province to obtain the spatial distribution characteristics and temporal evolution of soil and rockfill dams. In order to analyze the impact of water level changes on soil and rockfill dams, the highest Xiaolangdi Reservoir Dam was analyzed by combining with reservoir water level, rainfall, etc. Further, the time series prediction model sparrow search algorithm, Long Short-Term Memory, considering the moving average filter (MAF-SSA-LSTM), is proposed. After evaluating the model's accuracy, the dam body deformation is predicted and analyzed.

## 2. Study Area and Data

### 2.1. Study Area

Henan Province, located between longitude  $110^{\circ}21' \sim 116^{\circ}39'E$  and latitude  $31^{\circ}23' \sim 36^{\circ}22'N$ , is situated in the middle and lower reaches of the Yellow River. As of 2022, Henan Province has 28 large dams with a storage capacity of 6045 million  $m^3$ , including 25 soil and rockfill dams, accounting for 89.3% of the total number of large dams in Henan Province. They play an important role in large water conservancy projects in Henan Province [42]. In this

paper, 17 large soil and rockfill dams in Henan Province (Table 1) are used as examples to carry out the study, and the distribution is shown in Figure 1.

**Table 1.** Some large soil and rockfill dams in Henan Province.

Dam	Area	Dam Type
Xiaolangdi Reservoir Dam	Mengjin County	Clay-inclined core wall rockfill dam
Baisha Reservoir Dam	Yuzhou	Homogeneous soil dam
Luhun Reservoir Dam	Song County	Inclined wall soil and rockfill dam
Baiguishan Reservoir Dam	Lushan County	Homogeneous soil dam
Gusitan Reservoir Dam	Ye County	Clay core wall sand and pebble dam
Yanshan Reservoir Dam	Fangcheng County	Inclined wall soil and rockfill dam
Zhaopingtai Reservoir Dam	Lushan County	Thin clay sloping wall sand and cobble dam
Zhaikou Reservoir Dam	Lingbao City	Clay heart wall sand shell dam
Yahekou Reservoir Dam	Nanzhao County	Clay heart wall sand shell dam
Nanwan Reservoir Dam	Xinyang City	Clay heart wall sand shell dam
Shishankou Reservoir Dam	Luoshan County	Clay heart wall sand shell dam
Wuyue Reservoir Dam	Guangshan County	Clay heart wall sand shell dam
Pohe Reservoir Dam	Guangshan County	Clay heart wall sand shell dam
Nianyushan Reservoir Dam	Shangcheng County	Clay heart wall sand shell dam
Boshan Reservoir Dam	Queshan County	Clay heart wall sand shell dam
Songjiachang Reservoir Dam	Miyang County	Clay heart wall sand shell dam
Banqiao Reservoir Dam	Zhumadian City	Clay heart wall sand shell dam

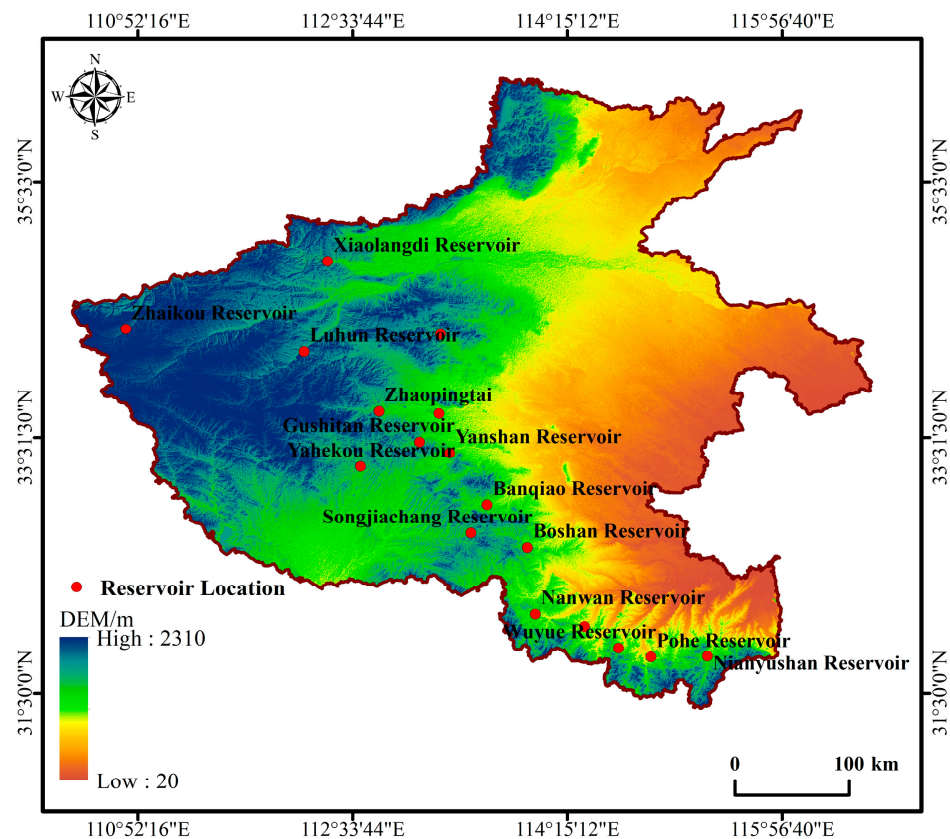


**Figure 1.** Schematic diagram of the geographical location of the study area.

## 2.2. Data Source

A total of 55 ascending orbit Sentinel-1A images covering the study area from March 2017 to September 2021 with an incidence angle of  $39.65^\circ$  (path 113) and  $39.72^\circ$  (path 40,11) at the dam position, precise orbit ephemerides data (POD), and Shuttle Radar Topography

Mission Digital Elevation Model (SRTM-1 DEM) were collected for deformation monitoring of large soil and rockfill dams in Henan Province to improve satellite orbit accuracy and remove terrain phase. The coverage is shown in Figure 2 [43]. The water level data of Xiaolangdi Reservoir Dam were obtained from the daily water conditions published on the official website of the Yellow River Conservancy Commission of the Ministry of Water Resources (<http://www.yrcc.gov.cn/>, accessed on 31 December 2022). The rainfall data were obtained from the monthly water conditions data published by the Henan Provincial Hydrology and Water Resources Measurement and Reporting Center (<http://www.hnssw.com.cn/>, accessed on 31 December 2022). These data were used to analyze the correlation between dam deformation, water level, and rainfall.

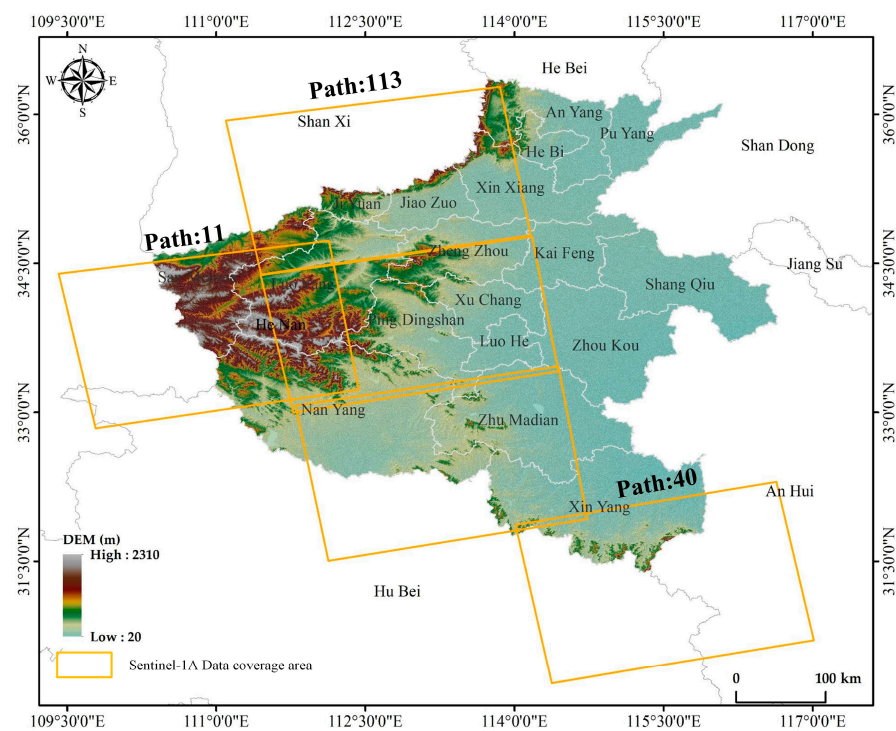


**Figure 2.** Sentinel-1A data coverage.

Meanwhile, the 171 Sentinel-1A images of Xiaolangdi Reservoir Dam from January 2017 to November 2022 were processed to obtain long-time series deformation. In order to increase the experimental accuracy and prevent accidental situations, multiple buffer zone with a radius of 5 m was established in the center of characteristic regions in the upper deformation area of the dam. All of the time series points were selected in the buffer to calculate the average value of each period deformation. It is combined into a set of data as the training dataset and validation dataset of the model. The first 80% of the experimental data are selected as the training set and the last 20% as the test set.

### 3. Methods

#### 3.1. PS-InSAR Technique

Ferretti et al. proposed the PS-InSAR technique in 2000, which effectively overcame the effects of temporal decorrelation and atmospheric delay errors [44]. The PS-InSAR technique is based on the identification of stable points with high reflectivity and little variation in space-time. By selecting a large number of PS points, the atmospheric delay phase can be estimated accurately, and the final deformation with millimeter accuracy is obtained. PS-InSAR mainly includes main image selection, co-registration, interference, inversion, geocoding and so on [45–47]. Its flow chart is shown in Figure 3.

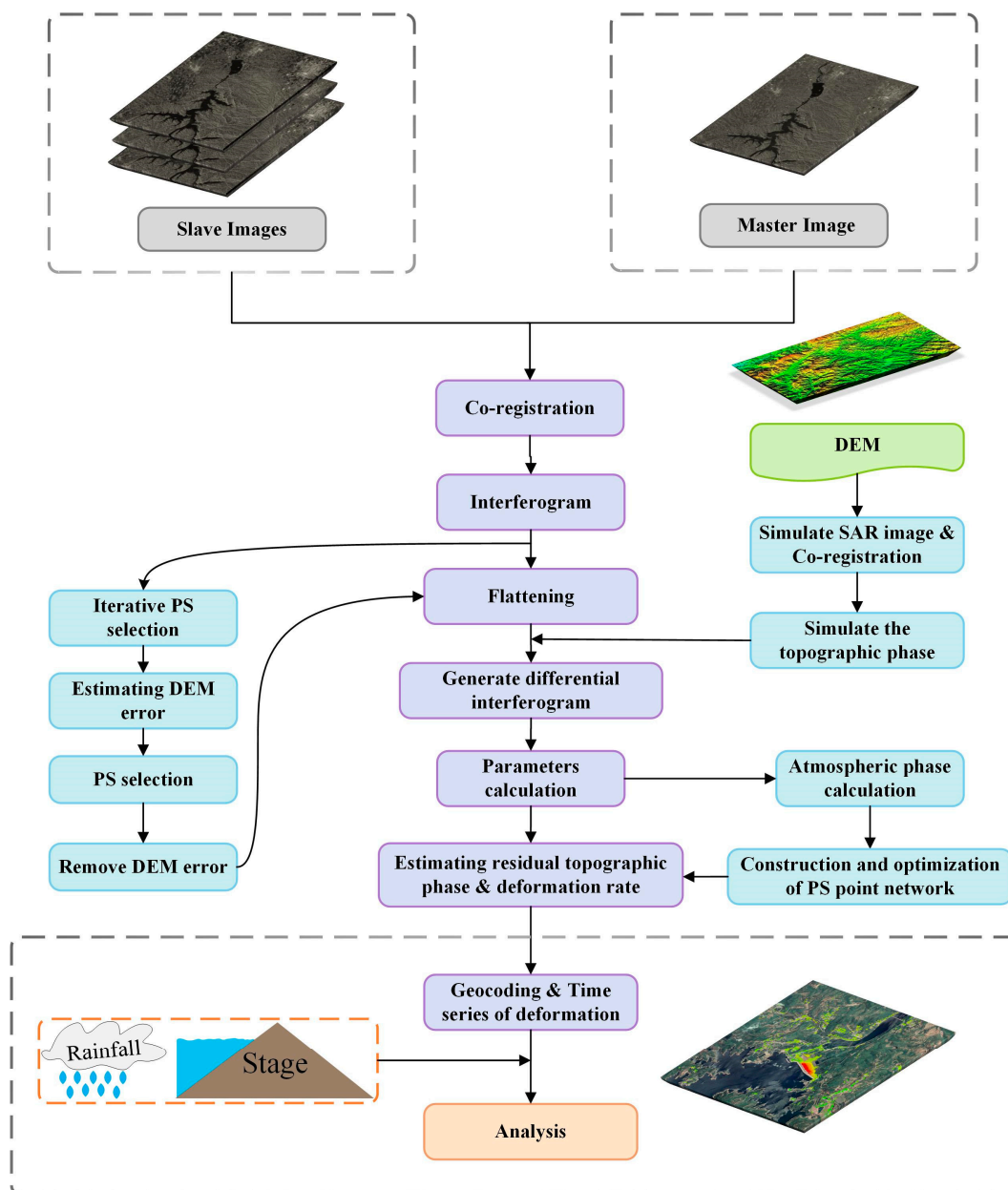


**Figure 3.** Flow chart of PS-InSAR processing.

Generally, the final results of InSAR are presented according to the deformation in the line-of-sight (LOS) direction, but the upstream slope dam and downstream slope dam of different soil and rockfill dams have different slopes. The different location directions of the dam body and the satellite incidence angle will lead to different local incidence angles of different slope dams, which will change the direction and size of the results [35]. The appearance of the dam body is similar to a multi-sided landslide. According to the characteristics of local earth rock materials and foundation geology, the slope angles of the upstream and downstream faces of the dam will be adjusted accordingly. Therefore, it is crucial to obtain the correct vertical deformation of slope dams for exploring the stability of soil and rockfill dams. Figure 4 shows the relationship between the true vertical deformation of soil and rockfill dam, slope, and incidence angle:

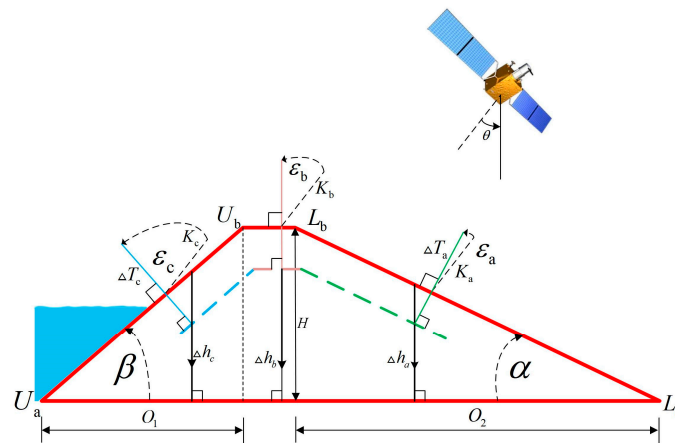


**Figure 4.** The relationship between the true vertical deformation of soil and rockfill dam, slope, and incidence angle.

$\epsilon_a, \epsilon_b, \epsilon_c$  is the incidence angle of different slope surfaces.  $H$  is the height of the dam.  $\Delta h_a, \Delta h_b, \Delta h_c$  is the true vertical deformation of the slope dam.  $\Delta T_a, \Delta T_c$  is the deformation perpendicular to the direction of the dam slope.  $O_1, O_2$  is the projection distance of the upstream and downstream slope dams on the level surface.  $K_a, K_b, K_c$  represents deformation along the satellite LOS. The formula for calculating the locality incidence angle of different slope dams is as follows in Equation (1):

$$\begin{cases} \epsilon_a = \theta - \alpha \\ \epsilon_b = \theta \\ \epsilon_c = \theta + \beta \end{cases} \quad (1)$$

where  $\theta$  is the satellite incidence angle, which will be provided in general image information,  $\alpha, \beta$  is the true slope angle of soil and rockfill dam, which are the ratio of  $H$  to  $O_1, O_2$ . Therefore, the true vertical deformation of the slope dam is shown in Equation (2).

$$\begin{cases} \Delta h_a = \frac{\Delta T_a}{\cos \epsilon_a} = \frac{K_a \times \cos \epsilon_a}{\cos \alpha} \\ \Delta h_b = K_b \times \cos \epsilon_b \\ \Delta h_c = \frac{\Delta T_c}{\cos \epsilon_c} = \frac{K_c \times \cos \epsilon_c}{\cos \beta} \end{cases} \quad (2)$$

It can be seen that the influence of the dam slope and incidence angle on the deformation results needs to be considered for the polyhedral slope building. Through the above calculation, the true vertical deformation of soil and rockfill dam can be obtained, and the dam deformation survey can be carried out more accurately.

### 3.2. MAF-SSA-LSTM Model

To solve the multi-objective function problem while improving the efficiency of model search, SSA-LSTM was used in this study, which is a new population optimization algorithm proposed by Xue et al. in 2020 [48]. The algorithm is based on the foraging and anti-predation behavior of the sparrow population. The sparrow population seeks the best place for food storage to realize the transformation of production and demand. This flexible behavior strategy optimizes the exploration and development of the search space. However, in the process of searching for the optimal solution by the sparrow, it is often difficult for the model to converge due to excessive boundary errors, making it difficult for the sparrow to search for the optimal solution. Therefore, it is necessary to perform “edge optimization” on the training data to improve its training efficiency.

In this study, the MAF-SSA-LSTM model is proposed, which shows great advantages in dealing with nonlinear problems, both in terms of convergence and accuracy. At the same time, the MAF algorithm is used to optimize the “outliers” in the SSA-LSTM network

structure locally to obtain the optimal boundary parameters, and the overall architecture of the model is shown in Figure 5.

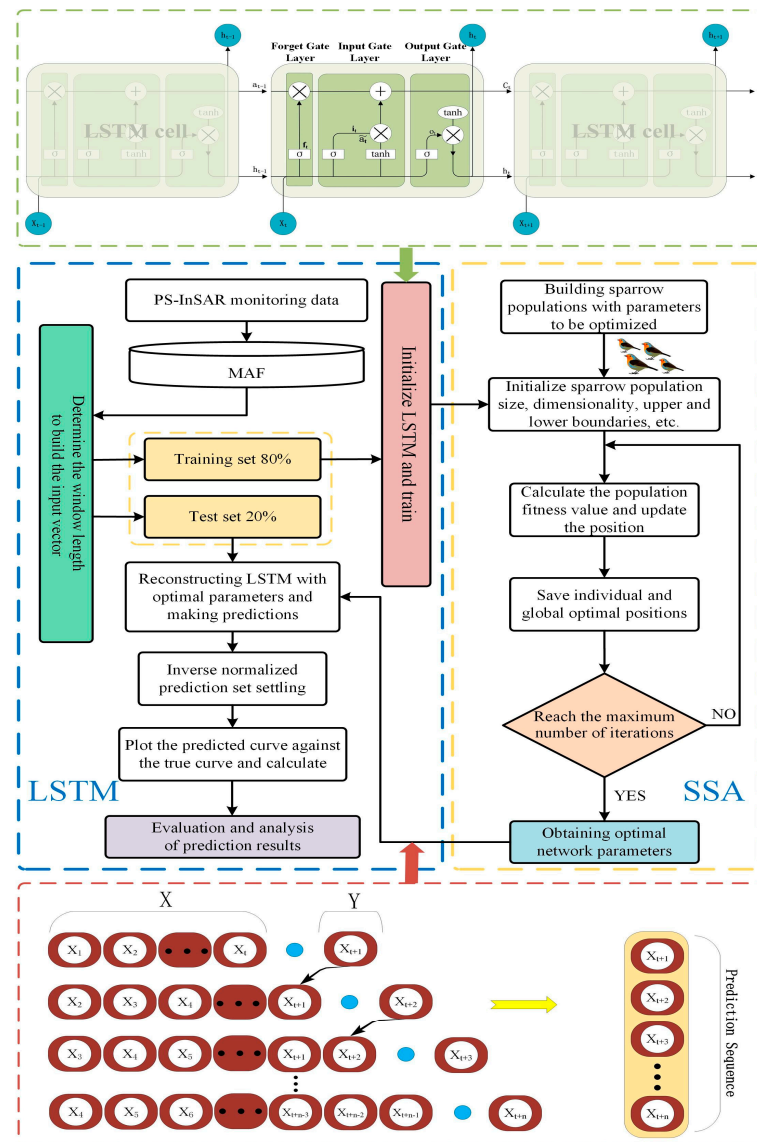


**Figure 5.** MAF-SSA-LSTM model structure.

According to Figure 5, it can be seen that the model optimization process involves the following three steps.

- (1) With the initial learning rate, regularization parameter, and the number of nodes in the hidden layer of the LSTM structure as the optimization objects, determine the sparrow population number, the maximum number of iterations, the number of optimization parameters, and the upper and lower bounds of parameter values (initial Learning rate, regularization coefficient, and the number of nodes in the hidden layer), and initialize the value of the SSA optimization algorithm.
- (2) Calculate the fitness value and update the position of each sparrow based on the number of sparrows in the population, and use Equations (6)–(8) to update the optimal individual position and global optimal position in the iterative sparrow population, and save the iteratively searched position.
- (3) Determine whether the maximum number of iterations has been reached. If so, exit the loop to obtain the optimal network parameters. Otherwise, continue with Step (2) above until the iteration ends and output the optimal network end parameters.

### 3.2.1. MAF

Because the deformation monitoring results of the InSAR technique are a nonlinear and non-stationary time series, in order to weaken the influence of some “outliers” in the deformation monitoring data on the whole deformation trend of the data, a moving average filter is used to smooth the data with a moving window length of 5, as shown in Equation (3).

$$\begin{aligned}
 yy(1) &= y(1) \\
 yy(2) &= (y(1) + y(2) + y(3))/3 \\
 yy(3) &= (y(1) + y(2) + y(3) + y(4) + y(5))/5 \\
 yy(4) &= (y(2) + y(3) + y(4) + y(5) + y(6))/5 \\
 yy(5) &= (y(3) + y(4) + y(5) + y(6) + y(7))/5 \\
 &\dots
 \end{aligned} \tag{3}$$

The obtained results are shown in Figure 6, and it can be found that the smoothed data better reflect the trend of dam deformation in the time series.

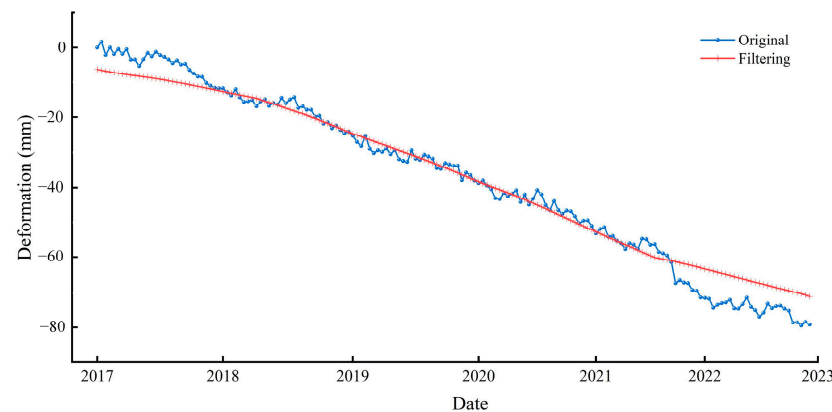


**Figure 6.** Comparison of original data and filtered data.

### 3.2.2. SSA

The SSA adopts the strategy of discoverers, joiners, and warners to simulate the foraging and anti-predatory behavior of sparrows. Assuming that the initial position of the sparrow population searching for food is represented by matrix  $X$ , and the fitness value of the population is represented by matrix  $F_X$ :

$$X = \begin{bmatrix} x_{1,1} & \cdots & x_{1,d} \\ \vdots & \ddots & \vdots \\ x_{n,1} & \cdots & x_{n,d} \end{bmatrix} \tag{4}$$

$$F_X = \begin{bmatrix} f([x_{1,1} \ \cdots \ x_{1,a}]) \\ \vdots & \ddots & \vdots \\ f([x_{n,1} \ \cdots \ x_{n,a}]) \end{bmatrix} \tag{5}$$

where  $n$  is the number of populations,  $d$  is the dimension of the variable, and each row of values in  $F_X$  represents the fitness value of the individual.

As the leader in searching for food in the population, the producer has a good fitness value. It guides the beggars to find food and is responsible for the migration of beggars. The location iteration process of the producer is as follows:

$$X_{i,j}^{t+1} = \begin{cases} X_{i,j}^t \cdot \exp\left(\frac{-i}{\alpha \cdot iter_{max}}\right), & R_2 < ST \\ X_{i,j}^t + Q \cdot L, & R_2 \geq ST \end{cases} \tag{6}$$

where  $t$  is the number of current iterations;  $X_{i,j}^t$  represents the value of the  $j$ -th dimension when the  $i$ -th sparrow iterates  $t$  times,  $j = 1, 2, \dots, d$ ;  $iter_{max}$  is a constant for the maximum number of iterations;  $\alpha \in (0, 1)$  of random numbers;  $Q$  is a normally distributed random number;  $L$  represent  $1 \times d$  matrix and all elements in the matrix are 1;  $R_2$  represents the alarm value;  $ST$  is the safety threshold. When  $R_2 < ST$ , it means that the producer can search for food in a wider area with no predators around. When  $R_2 \geq ST$ , it represents the producer's detection of danger and the need to direct the sparrow population to a safe area.

As the beggars in the population have lower fitness values, they need to continuously pay attention to the dynamics of the producers. If the producers find better food, the beggars will quickly compete for it. If the competition fails, the beggars will continue to monitor the dynamics of the producers. Therefore, the position iteration of the beggars is as follows:

$$X_{i,j}^{t+1} = \begin{cases} Q \cdot \exp\left(\frac{X_{worst}^t - X_{i,j}^t}{i^2}\right), & i > \frac{n}{2} \\ X_p^{t+1} + |X_{i,j}^t + X_p^{t+1}| + A^+ \cdot L, & \text{Others} \end{cases} \quad (7)$$

where  $X_p$  represents the latest food position found by the producer,  $X_{worst}$  represents the current worst position,  $A$  represents a matrix of  $1 \times d$  with elements randomly assigned as either 1 or  $-1$ , and  $A^+ = A^T(AA^T)^{-1}$ . When  $i > \frac{n}{2}$ , it represents the unfavorable fitness value of the  $i$ -th beggar in the population.

When danger is detected, the birds on the periphery of the population will quickly move to a safe area, while those in the middle will randomly move. The position iteration of the safety-conscious sparrows in the population that search for safe locations is as follows:

$$X_{i,j}^{t+1} = \begin{cases} X_{best}^t + \beta \cdot |X_{i,j}^t - X_{best}^t|, & f_i > f_g \\ X_{i,j}^t + K \cdot \left(\frac{|X_{i,j}^t - X_{worst}^t|}{(f_i - f_p) + \varepsilon}\right), & f_i = f_g \end{cases} \quad (8)$$

where  $X_{best}$  is the current best fitness position,  $\beta$  represents the step size control parameter, which is a random number following a normal distribution with a mean of 0 and a variance of 1,  $K$  represents a random number in the interval  $[-1, 1]$ , which represents the direction and coefficient of movement of the step size of the sparrows in the population,  $f_i$  represents the fitness value of the  $i$ -th sparrow,  $f_g$  represents the global best fitness value,  $f_p$  represents the global worst fitness value, and  $\varepsilon$  represents a constant close to 0 to avoid zero division errors.  $f_i > f_g$  represents a sparrow located on the outer edge of the population, which needs to move to a safe location when danger is detected;  $f_i = f_g$  represents sparrows in the middle area of the population who are aware of the danger and need to search for a safe location.

The SSA utilizes the danger awareness of the sparrow population and iteratively updates the latest positions of all sparrows in the population using Equations (6)–(8). Based on the position information of the sparrow population, the optimal individual position and global optimal fitness value in the population are obtained, thereby determining the optimal weights and thresholds of the LSTM model.

#### 4. Results

Deformation monitoring was conducted on 17 dams in Henan Province using the PS-InSAR technique. The cumulative deformation maps of each dam from March 2017 to September 2021 were obtained, as shown in Figure 7. The red ellipse represents the location of the master dam for each soil and rockfill dam.

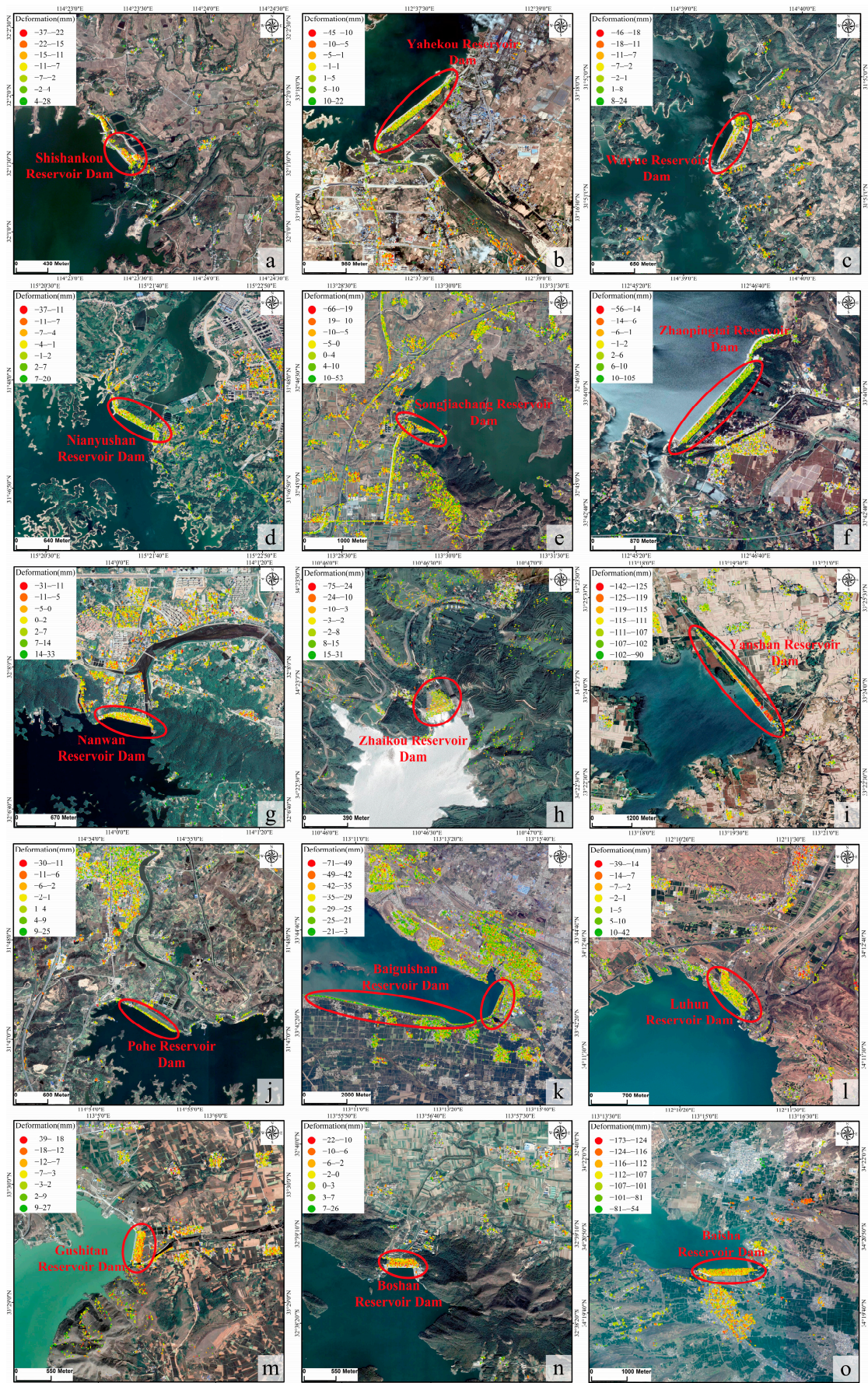
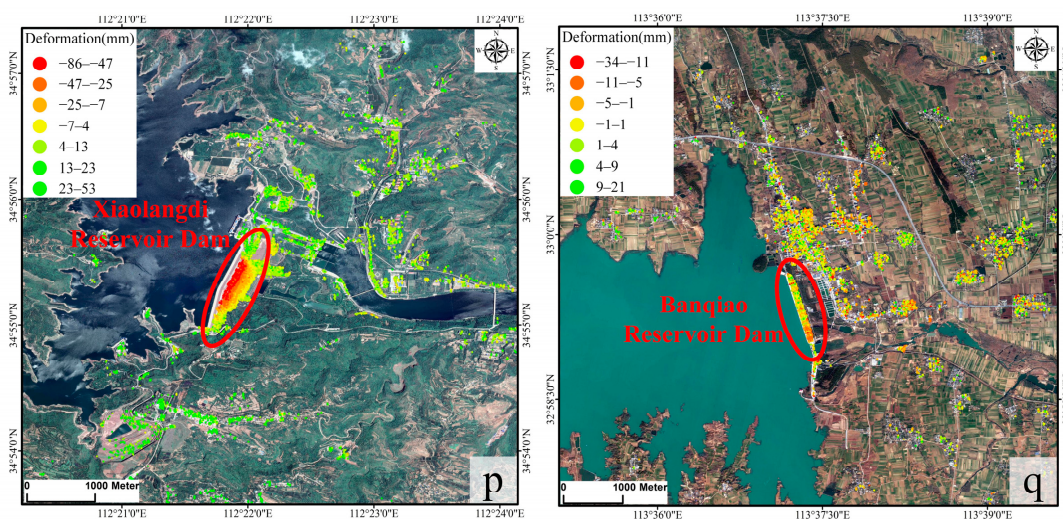


Figure 7. Cont.



**Figure 7.** Deformation of large soil and rockfill dams in Henan Province. (a) Shishankou Reservoir Dam; (b) Yahekou Reservoir Dam; (c) Wuyue Reservoir Dam; (d) Nianyushan Reservoir Dam; (e) Songjiachang Reservoir Dam; (f) Zhaopingtai Reservoir Dam; (g) Nanwan Reservoir Dam; (h) Zhaikou Reservoir Dam; (i) Yanshan Reservoir Dam; (j) Pohe Reservoir Dam; (k) Baiguishan Reservoir Dam; (l) Luhun Reservoir Dam; (m) Gushitan Reservoir Dam; (n) Boshan Reservoir Dam; (o) Baisha Reservoir Dam; (p) Xiaolangdi Reservoir Dam; (q) Banqiao Reservoir Dam.

Through deformation monitoring results, it can be observed that among the 17 large-scale soil and rockfill dams in Henan Province, there are three dams with relatively small deformation: The deformation on both sides of the Wuyue Reservoir dam is relatively small, with slight deformation in the middle. The Pohe Reservoir Dam and Nanwan Reservoir Dam show slight overall deformation, reaching  $-46$  mm,  $-30$  mm, and  $-31$  mm, respectively. The left side of the Yahekou Reservoir Dam demonstrates an upward trend, and the right side displays distinct evidence of subsidence, reaching  $-45$  mm. Dams with severe deformation on the left side include Songjiachang Reservoir Dam, Zhaopingtai Reservoir Dam, and Banqiao Reservoir Dam, reaching  $-66$  mm,  $-56$  mm, and  $-34$  mm, respectively. Dams with deformation in the middle include Luhun Reservoir Dam and Gushitan Reservoir Dam, both reaching  $-39$  mm. Dams with deformation on both sides include Nianyushan Reservoir Dam, reaching  $-37$  mm. Dams with severe deformation on the top include Zhaikou Reservoir Dam and Boshan Reservoir Dam, reaching  $-75$  mm and  $-22$  mm, respectively. Dams with overall deformation include Shishankou Reservoir Dam and Baiguishan Reservoir Dam, reaching  $-37$  mm and  $-71$  mm, respectively, and the most severe deformation can be found in Xiaolangdi Reservoir Dam, Yanshan Reservoir Dam, and Baisha Reservoir Dam, reaching  $-86$  mm,  $-142$  mm, and  $-173$  mm, respectively. The deformation of the middle part of Xiaolangdi Reservoir Dam is larger than that of the dam abutment on both sides. The deformation on the left side of Yanshan Reservoir Dam is serious, and the deformation decreases from left to right. The overall deformation of the Baisha Reservoir Dam is serious. From the deformation monitoring results, it can be found that all 17 large-scale soil and rockfill dams in Henan Province have various degrees of deformation. Therefore, it is important to pay close attention to these water conservancy projects.

Analysis from soil and rockfill dam materials and anti-seepage structure types, soil and rockfill dams can be roughly divided into three categories: homogeneous dams, sloping wall dams, and core wall dams. Among them, core wall dams are the most commonly used type for large reservoirs in Henan Province. They feature a seepage control structure located in the center of the dam, with the sides of the dam slope supporting and protecting the internal core wall. This design provides a stable structure and good seismic performance, making it unique compared with the other two types of soil and rockfill dams. According

to the monitoring results, the deformation degree of dams with core walls is often smaller than that of dams without core walls. Because the soil mass in the core wall area is solid, and the gap is very small. Moreover, the core wall has the characteristics of low seepage, which can well block the water seepage to retard the deformation of the soil layer. Among the soil and rockfill dams studied, the Baisha Reservoir Dam is a homogeneous earth dam with severe consolidation effects and the highest annual deformation rate, followed by the inclined wall soil and rockfill dam, Yanshan Reservoir Dam. Clay heart wall sand shell dams are a relatively stable type of dam. The clay core sand shell dam employs low-permeability viscous soil as the seepage control material in the middle of the dam. Due to its good stability, this type of dam is widely used in the construction of large-scale soil and rockfill dams. In fact, the proportion of clay core sand shell dams in the large-scale soil and rockfill dams studied in this study reached 64.7%.

A buffer zone with a radius of 5 m is established around severe deformation zones of 17 soil and rockfill dams to improve experimental accuracy and prevent accidental errors. The average deformation of all points in the buffer zone is selected for mapping. Figure 8a,b represents the relationship between the height of soil and rockfill dams with core wall and the deformation, and the relationship between soil and rockfill dams with different materials and deformation. In Figure 8a, the blue mark represents the height of the soil and rockfill dam, and the red ellipsoid represents the deformation of the soil and rockfill dam. It can be found that the height and deformation trend of soil and rockfill dam with the core wall are basically the same. The Boshan Reservoir Dam is only abnormal because it was built in 1954, 70 years ago. In such a long period of time, the soil mass is compacted under the influence of gravity, and the porosity between particles of bulk earth rock becomes smaller, so the deformation is not serious. The Xiaolangdi Reservoir Dam, with the highest height of 160 m, and the narrow-mouthed reservoir dam, with the second highest height of 77 m, both have experienced significant deformation. The former, as the highest soil and rockfill dam in Henan Province, should be a key area of concern, and Section 5 of this study will focus on its analysis. In Figure 8b, both the homogeneous dam and inclined wall dam have abnormal deformation. The Baisha Dam, a homogeneous dam, has reached  $-173$  mm, and the Yanshan Dam, an inclined wall dam, has reached  $-142$  mm, but the Xiaolangdi Dam, a core wall dam, has only  $-86$  mm. This is because the homogeneous dam is horizontally compacted in layers, and the permeability of the soil is non-uniform, forming a high saturation line in the dam body. Therefore, it can cause the soil to soften or mud, thereby causing significant deformation. The abnormal deformation of the inclined wall dam may be caused by the small contact stress between the inclined wall and the foundation, poor bonding with the foundation, and poor permeability of the material itself. Compared with the above two types of dams, the core wall has excellent low permeability and low deformation characteristics. Therefore, the deformation of the core wall dam is the smallest and positively correlated with its own dam height. Therefore, more excellent core wall dams in terms of structure and materials should be given special attention.

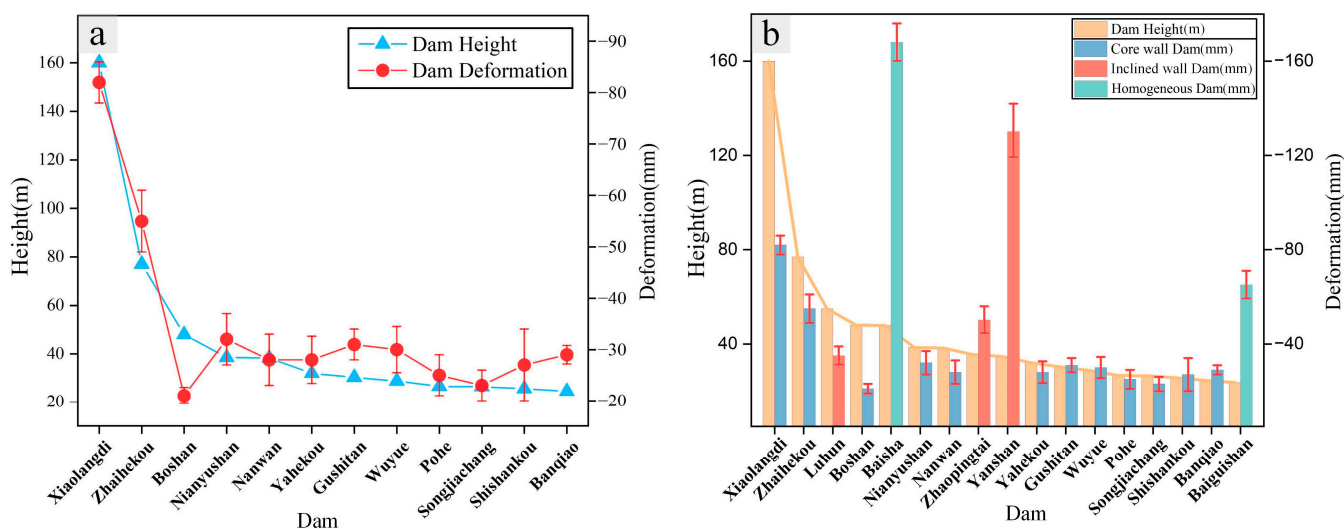


**Figure 8.** (a) Soil and rockfill dam with core wall and height; (b) three soil and rockfill dam types and deformation.

We evaluated the safety status of 17 soil and rockfill dams in the study area according to the cumulative deformation of large soil and rockfill dams in Henan Province from March 2017 to September 2021 and requirements in the local “Design code for rolled soil and rockfill dams” (SL274-2020) [49]. In order to prevent excessive deformation, the dam crest needs to reserve deformation superelevation, in which the superelevation value of the soil impervious dam body is 2% of the design height of the dam body. For a 100 m high soil and rockfill dam, the allowable value of deformation after construction is 2000 mm. Dams with cumulative deformation greater than 100 mm in the study area include the Baisha Reservoir Dam and the Yanshan Reservoir Dam. Dams with deformation between 50 mm and 100 mm include the Xiaolangdi Reservoir Dam, Zhaikou Reservoir Dam, Songjiachang Reservoir Dam, Zhaopingtai Reservoir Dam, and Baiguishan Reservoir Dam. Dams with deformation less than 50 mm include the Wuyue Reservoir Dam, Yahekou Reservoir Dam, Gushitan Reservoir Dam, Luhun Reservoir Dam, Nianyushan Reservoir Dam, Shishankou Reservoir Dam, Banqiao Reservoir Dam, Nanwan Reservoir Dam, Pohe Reservoir Dam, and Boshan Reservoir Dam.

The deformation results of 17 dams are far less than the allowable deformation range. Only the Baisha Reservoir Dam and Yanshan Reservoir Dam have large deformation. It is found that there are a large number of coal mining enterprises around the Baisha Reservoir. Underground mining of coal mines can lead to serious surface subsidence. Meanwhile, coal mining enterprises need to pump a large amount of groundwater for production and life. All of them may result in the overall deformation of the reservoir. The Yanshan Reservoir Dam is mainly constructed by a homogeneous soil dam, and the groundwater drainage condition on the dam base is poor, so the dam will have serious seepage deformation under the condition of long-term water storage. Secondly, the area of expansive soil in the reservoir area is large, which will affect the deformation and stability of the dam after the impoundment of the reservoir. Thirdly, there are many villages around the reservoir with dense personnel activities. The villagers’ daily water and a large amount of groundwater exploitation will also cause the overall subsidence of the surrounding area. However, the deformation result is still within the safe range. Moreover, both dams have adopted reinforcement measures. Therefore, all 17 dams are in a safe state.

## 5. Discussion

### 5.1. Deformation Monitoring Analysis of Xiaolangdi Soil and Rockfill Dam

The Xiaolangdi Water Control Project is located at the exit of the Yellow River gorge in the middle reaches of the river, within the Xiaolangdi area of Mengjin County, Henan

Province. The dam adopts a clay-inclined core wall rockfill dam with a maximum height of 160 m and a length of 1667 m. There is an 8 m-wide raceway at the top of the dam, with an upstream slope of 1:1.75 and a downstream slope of 1:2.6. The Xiaolangdi Dam is currently the largest soil and rockfill dam in Henan Province, with a filling capacity of 51.85 million m<sup>3</sup> and a storage capacity of 12.65 billion m<sup>3</sup> [50]. Figure 9 provides a clear overview of the study area.

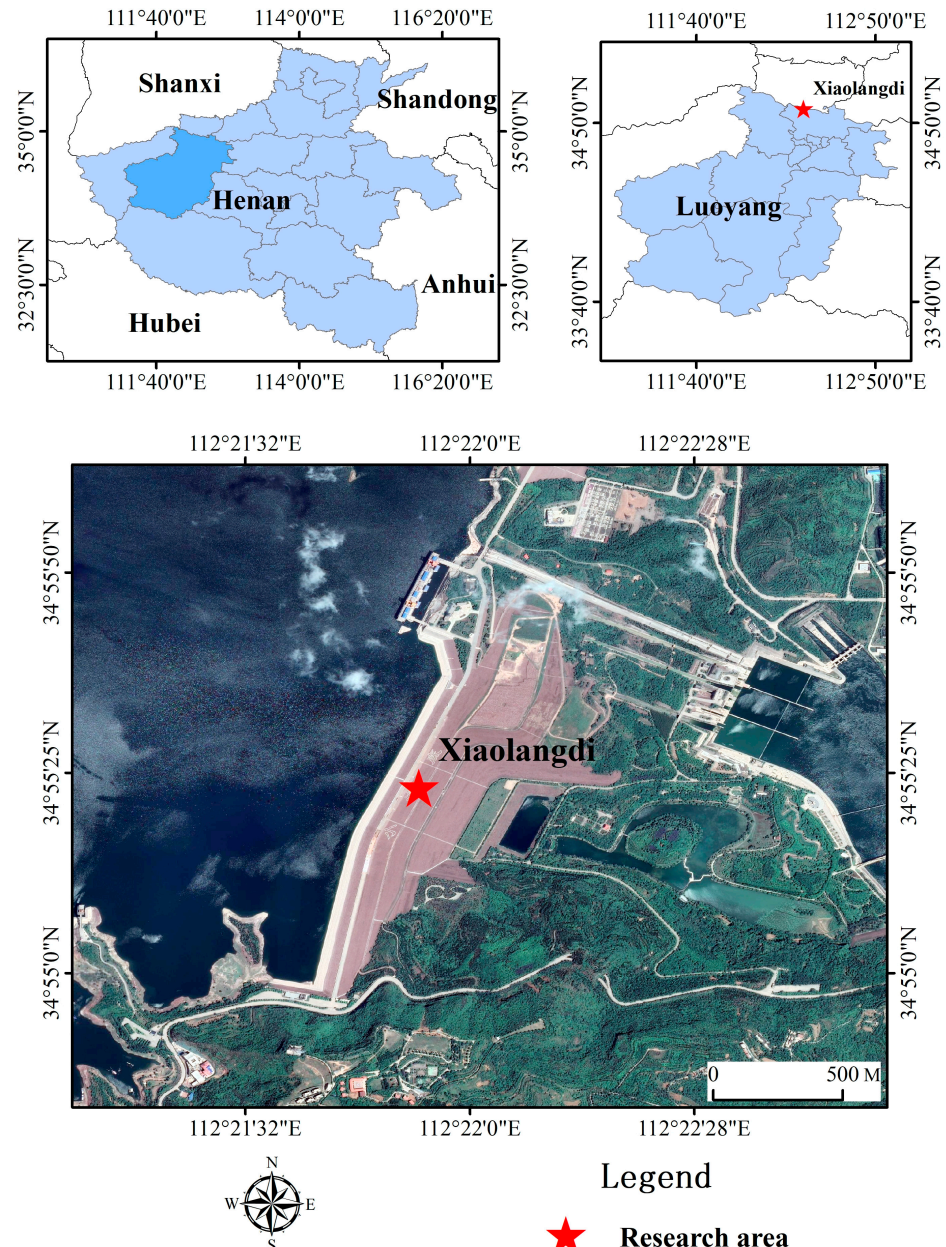


**Figure 9.** Overview map of the study area.

This experiment utilized the PS-InSAR technique to process 55 Sentinel-1A images, generating an average deformation map of the Xiaolangdi Reservoir Dam from March 2017 to September 2021 in the line-of-sight direction. Based on the degree of deformation observed during different time periods, the deformation of the dam body was statistically analyzed, as shown in Figure 10. Negative values indicate movement away from the satellite direction and represent the deformation of the dam body. In contrast, positive values indicate movement towards the satellite direction and represent the rise of the dam body. It can be observed from the figure that the PS points are mainly concentrated on the

dam body of the reservoir. The deformation of the Xiaolangdi Reservoir Dam decreases gradually from the top to the bottom, with the central part exhibiting greater deformation than the two sides. The maximum cumulative deformation recorded reaches  $-86.09$  mm.

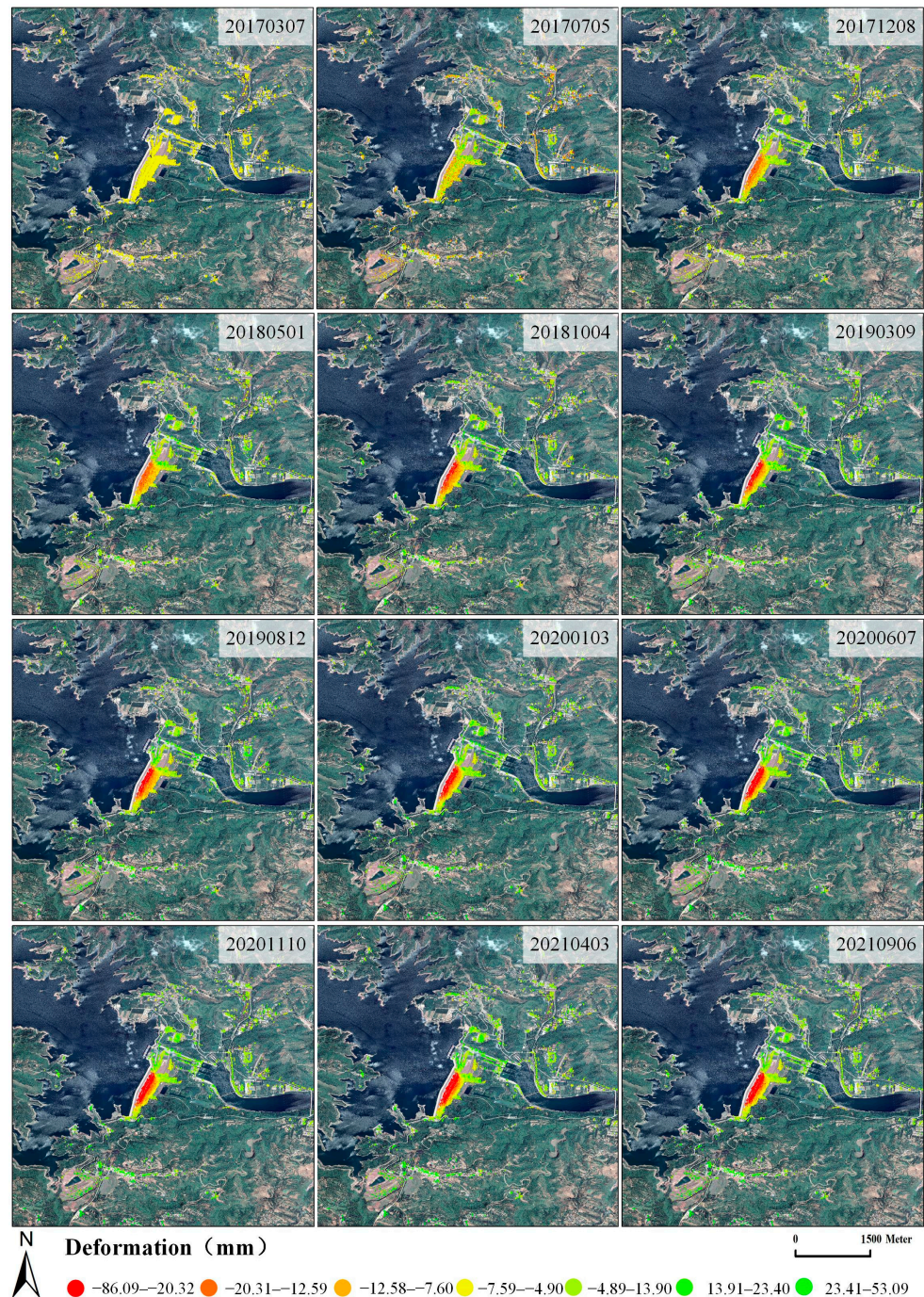


**Figure 10.** Cumulative deformation in LOS direction of Xiaolangdi Reservoir Dam at each stage.

Beginning in March 2017, it took about nine months for significant deformation to appear at the top of the dam in December 2017. Subsequently, noticeable stepped shape deformation was observed in March 2019, and this pattern continued in the following time periods. These findings indicate that the Xiaolangdi Reservoir Dam has undergone significant deformation over approximately two years.

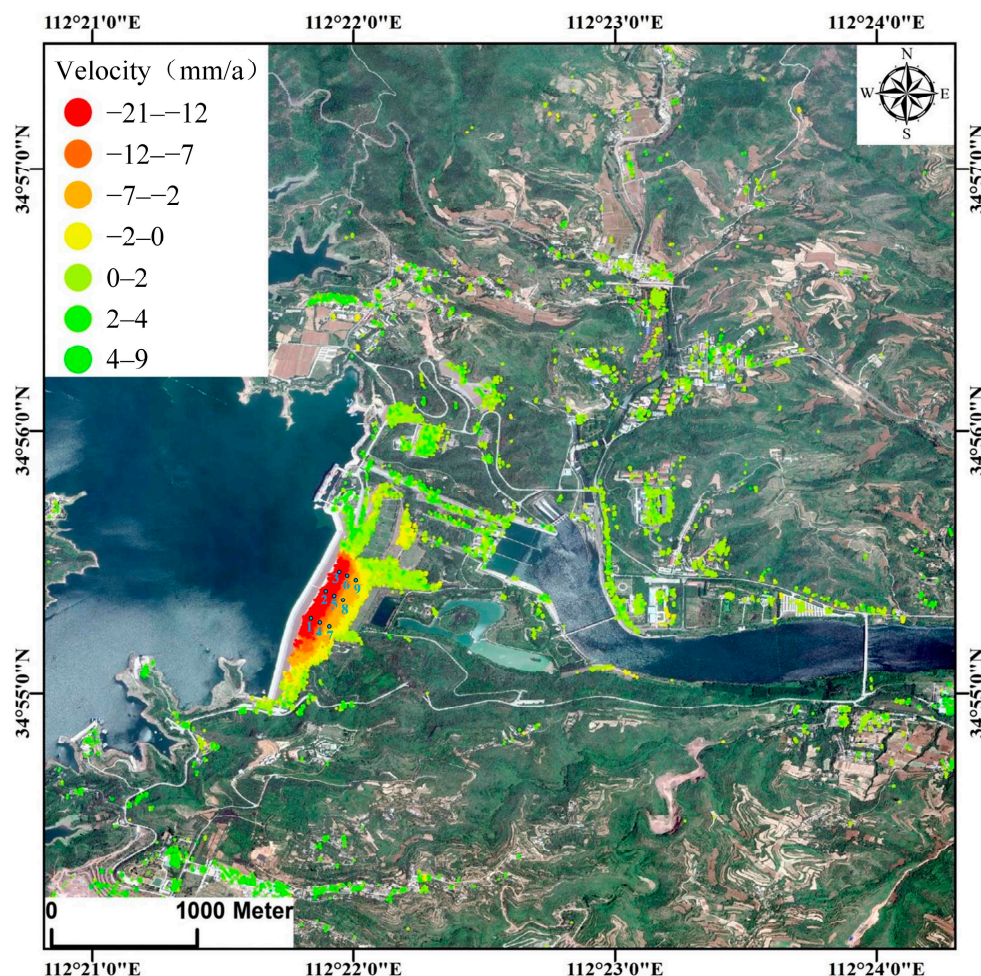
Based on the deformation monitoring results of the Xiaolangdi Reservoir Dam, a detailed analysis was conducted on the critical parts of the dam body and the deformation

of its longitudinal-transverse section. As shown in Figure 11, the critical areas of the dam body were designated, along with longitudinal section B-B1 and transverse section A-A1, and critical monitoring points were set at positions 1–19.



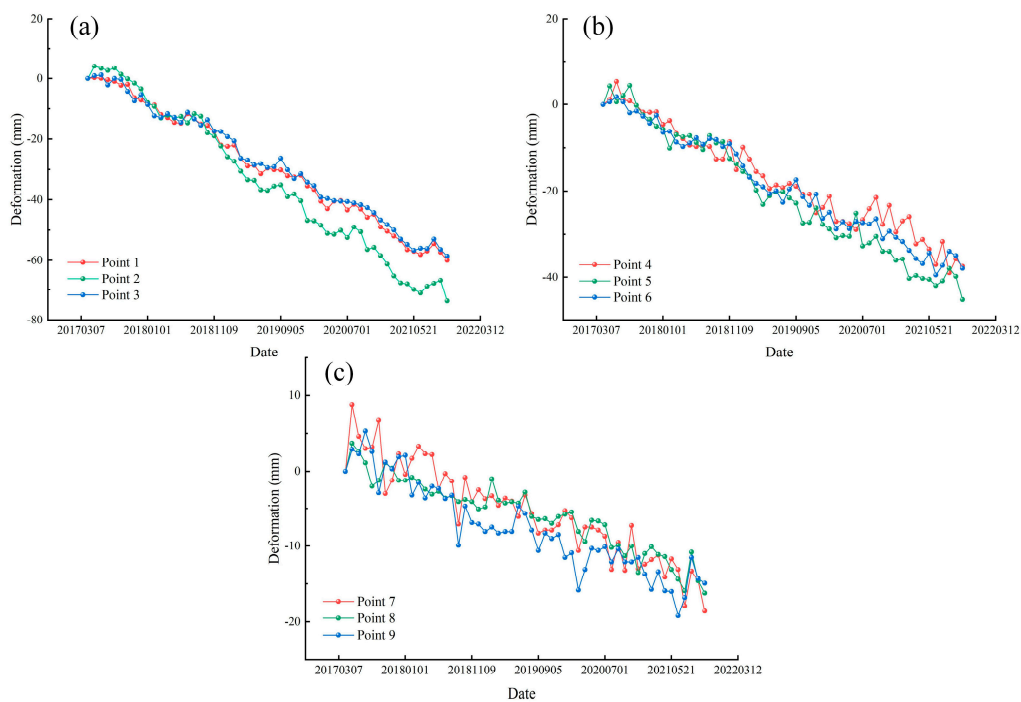
**Figure 11.** Transverse and longitudinal sections and the distribution of key points.

The displacement obtained by satellites is only deformation perpendicular to the slope surface. The upstream and downstream slope dams are not in the same direction as the deformation of the dam crest, resulting in deformation deviation. The above method, as Section 3.1 in this study, was used to convert the vertical deformation of different slope dam surfaces to vertical to the level surface. For the Xiaolangdi soil and rockfill dam, the upstream slope dam has less deformation information due to the influence of the storage level, slope, and incidence angle. So, the deformation of the downstream slope dam perpendicular to the level surface is mainly considered, and the deformation of the dam crest and the downstream slope dam is converted to the same direction to improve the reliability of the analysis results. The transformed deformation rate diagram is shown in Figure 12. Points 1 to 3 with deformation rates ranging from  $-21$  mm/a to  $-12$  mm/a; points 4 to 6 with deformation rates ranging from  $-12$  mm/a to  $-7$  mm/a; and points 7 to 9 with deformation rates ranging from  $-7$  mm/a to  $-2$  mm/a.



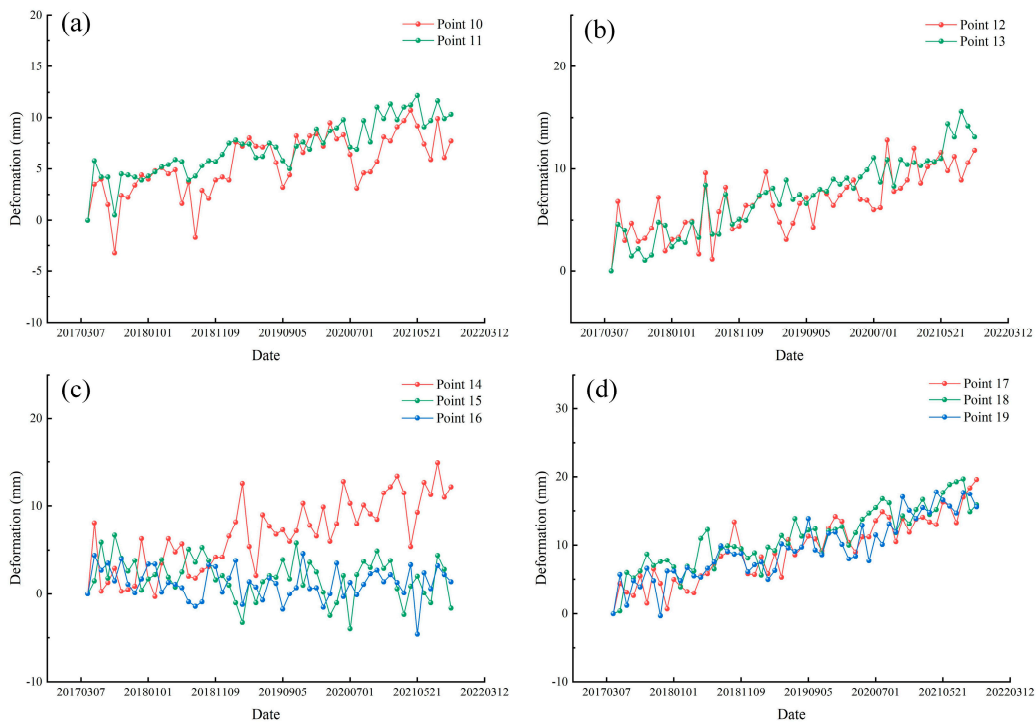
**Figure 12.** The deformation rate of the Xiaolangdi Reservoir Dam vertical to the level surface.

Figure 13a revealed that the upper part of the Xiaolangdi Reservoir Dam had experienced a deformation of approximately 80 mm over the past five years, showing a downward trend and a more linear deformation curve. This indicates that the deformation in the upper part of the dam is periodic. The middle section of the dam exhibited a deformation of approximately 40 mm, which is relatively slow in comparison with the upper part and reveals slight oscillations, as illustrated in Figure 13b. On the other hand, Figure 13c highlights that the lower part of the dam has sunk by around 20 mm, and the deformation consistently exhibits a high magnitude of oscillation. Overall, the deformation of the Xiaolangdi Reservoir Dam gradually diminishes from top to bottom. This can be attributed to two reasons: Firstly, the dam's significant weight contributes to noticeable deformation in the upper part. It follows that being a large-scale soil and rockfill dam, the long-term accumulation of soil and rock materials causes soil compaction, leading to distinct diminishing deformation from the top to the bottom. As the lower part of the dam is beneath the reservoir water level, the magnitude of the deformation is influenced by the water pressure generated due to fluctuations in the reservoir's water level. This explains why the deformation magnitude of points 4 to 6 is relatively minor in comparison with points 7 to 9.



**Figure 13.** (a) Deformation at points 1, 2, and 3 in the upper part of Xiaolangdi Dam; (b) deformation at points 4, 5, and 6 in the middle of Xiaolangdi Dam; (c) deformation at points 7, 8, and 9 in the lower part of Xiaolangdi Dam.

The rest of the monitoring points, consisting of points 10 through 19, are distributed as follows: points 10 and 11 at the base of the dam, points 12 and 13 at the left abutment, points 14 to 16 at the right abutment, and points 17 to 19 at the spillway. Points 10 and 11 at the dam's base exhibit a similar uplift trend, but point 11 has a greater magnitude than point 10, as depicted in Figure 14a. Points 12 and 13 at the left abutment have experienced a 10 mm uplift on average over the past five years. The outer point 12 experienced higher deformation than the inner point 13, as shown in Figure 14b. Points 14 to 16 at the right abutment display a comparable deformation pattern, with points 15 and 16 oscillating around zero while monitoring point 14, located on the outer side of the right abutment, undergoes a relatively significant uplift with a similar trend in deformation, as shown in Figure 14c. Finally, points 17 to 19 at the spillway have experienced an average uplift of around 15 mm in the past five years. They continuously oscillate due to water pressure during flood discharge, as shown in Figure 14d. The Xiaolangdi Dam displays unique deformation characteristics at each monitoring point compared to other areas. The right side of the dam is relatively stable compared with the left, where more noticeable deformation occurs on the outer side of the abutment. Meanwhile, the dam base remains relatively stable with lower levels of deformation. In contrast, the spillway shows obvious deformation due to long-term water flow impact and displays a further regular pattern.



**Figure 14.** (a) Deformation at points 10 and 11 at the bottom of Xiaolangdi Dam; (b) deformation at points 12 and 13 at the left shoulder of Xiaolangdi Dam; (c) deformation at points 14, 15, and 16 at the right shoulder of Xiaolangdi Dam; (d) deformation at points 17, 18, and 19 at the floodgate of Xiaolangdi Dam.

We further analyze the section of the Xiaolangdi Dam, specifically cross-section A-A1 in Figure 15a and longitudinal-section B-B1 in Figure 15b. It appears that the middle section of the dam has experienced larger deformation in the past five years compared with the sides. The maximum deformation reached 86 mm, while the right side of the dam was relatively stable compared with the left. Moreover, Figure 15b shows that the deformation of the Xiaolangdi Dam decreases progressively from the top to the bottom of the dam in the vertical direction. This implies that the soil and rockfill dam undergoes more significant deformation due to factors such as water pressure and gravity at higher elevations, necessitating closer monitoring of the top of the dam.

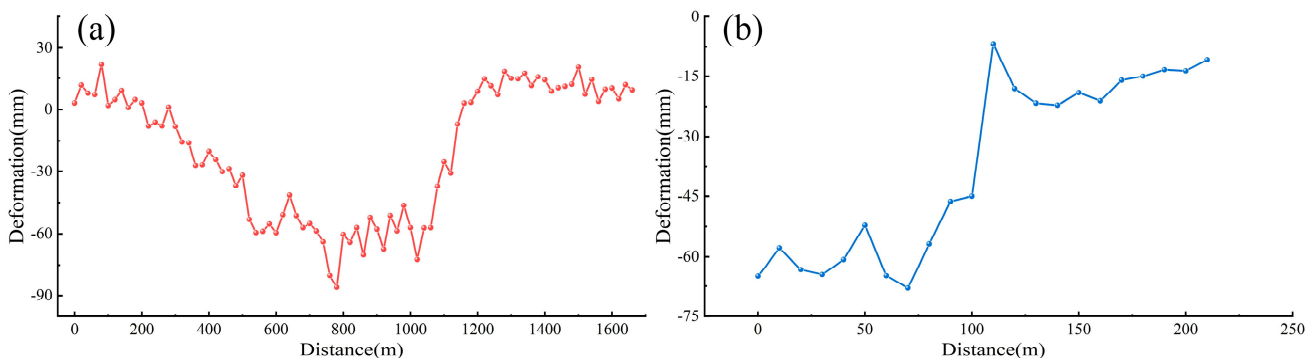


**Figure 15.** (a) Cross-section A-A1 of Xiaolangdi Reservoir Dam; (b) cross-section B-B1 of Xiaolangdi Reservoir Dam.

### 5.2. Correlation Analysis of Reservoir Water Level, Rainfall and Deformation

The Xiaolangdi Dam was analyzed based on the deformation of five randomly selected points, as shown in Figure 16. The dam deformation trend exhibits a stepped shape. Moreover, the upstream water level of the Xiaolangdi Reservoir undergoes annual cyclical

changes. As the water level continuously varies, the dam deformation trend becomes more apparent during high water levels and slower during low water levels. This suggests that the water level plays a critical influence on the deformation behavior of the dam. From the analysis in Figure 16, during the stages of ① → ②, ③ → ④, ⑤ → ⑥, ⑦ → ⑧, and ⑨ → ⑩, the deformation curve slope was steeper, indicating a higher deformation rate. During these stages, the water level of the reservoir is in a state of rising or falling. However, during the stages of ② → ③, ④ → ⑤, ⑥ → ⑦, and ⑧ → ⑨, the slope of the change curve was small, the deformation rate was slower, and the reservoir water level was in a storage state, causing less significant deformation. This illustrates that the water level has an impact on the deformation of the dam. In addition, during the stage of ⑨ → ⑩, Henan Province experienced an unprecedented extreme weather event with rainfall exceeding the historical maximum of the past five years. The water level of the reservoir has rapidly increased, and the Xiaolangdi Dam has also experienced abnormal deformation with a sharp decrease (slope significantly greater than the previous four years) compared with the same period in previous years.

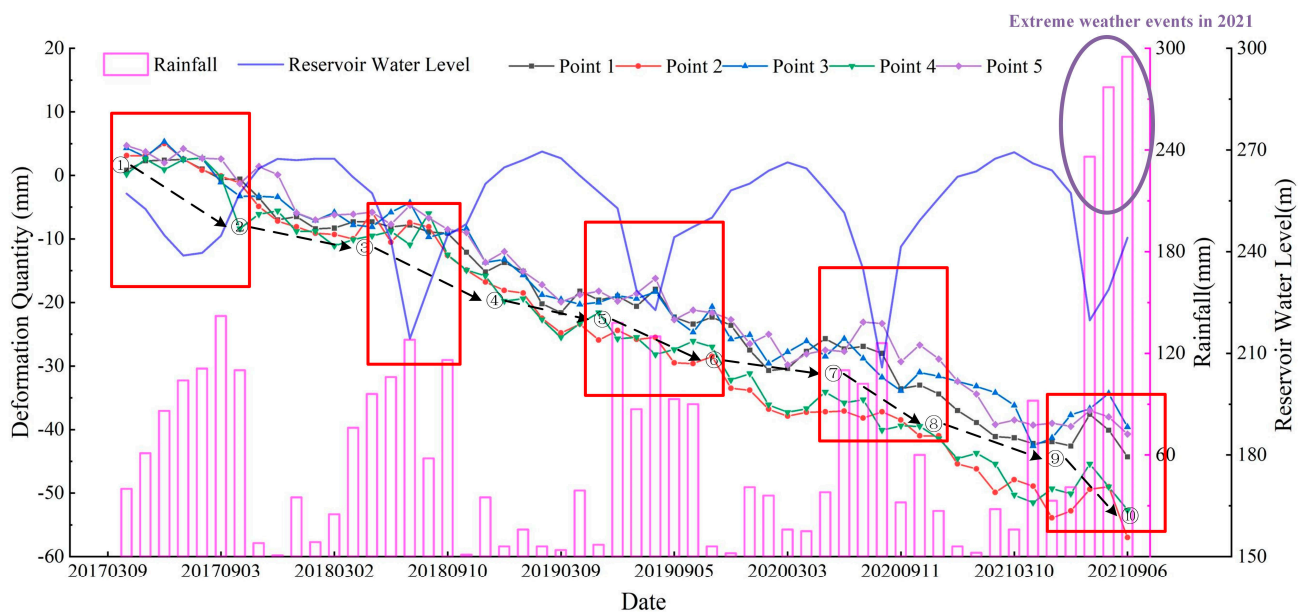


**Figure 16.** Relationship between rainfall, reservoir level, and deformation of Xiaolangdi Reservoir Dam.

The research area is located near  $34^{\circ}55'N$  and belongs to the warm temperate zone, with a continental monsoon climate throughout the year. It has the characteristics of distinct four seasons, simultaneous rainfall and heat, complex diversity, and frequent climate disasters. Summer rainfall is high, while winter rainfall is small and intermittent. The annual rainfall is concentrated from July to September, with the characteristics of concentrated rainfall and large instantaneous rainfall, which can easily cause short-term rapid rise of reservoir water level, especially in July to September 2021, with an average monthly rainfall of 280 mm. Meanwhile, it can be observed that during the low water level stages ① → ②, ③ → ④, ⑤ → ⑥, ⑦ → ⑧, ⑨ → ⑩, it is in summer, with more local rainfall and a larger slope, resulting in accelerated deformation, as shown in the red box in Figure 16. During the stages of ② → ③, ④ → ⑤, ⑥ → ⑦, ⑧ → ⑨, when the water level continues to rise, it is in winter. The local rainfall is relatively low, the slope is small, and the deformation slows down. The seasonal characteristics of dam deformation are significant. Therefore, soil and rockfill dam generally presents the deformation law of “quick summer and slow winter” with distinctive seasonal characteristics.

From mid-June through early July each year, the Xiaolangdi Reservoir opens its gates to discharge water to adjust the water and sediment of the Yellow River basin. During

this period, the reservoir water level drops by approximately 50 m. Figure 16 shows that after the discharge process, the deformation rate of the Xiaolangdi Dam slows down, and a slight uplift occurs.

Through correlation analysis of water level, rainfall, and dam deformation trend, it is shown that the difference in water level has a significant disturbance on dam deformation, and rainfall indirectly affects dam deformation. Regular fluctuations can be observed in the dam's deformation as the water level continues to rise or fall.

### 5.3. Results and Accuracy Evaluation of MAF-SSA-LSTM Model

The MAF-SSA-LSTM model was optimized using the Adam optimizer in this experiment. The sparrow population size was fixed at 20, with a population dimension of 3. The initial learning rate was set within the range of  $[1 \times 10^{-3}, 1 \times 10^{-2}]$ , while the regularization coefficient and the number of nodes in the hidden layer were limited to  $[1 \times 10^{-4}, 1 \times 10^{-1}]$  and  $[10, 30]$ , respectively. The model was trained for a maximum of 8 iterations, undergoing a total of 1000 training cycles.

Following the experimental process above, the deformation data of Xiaolangdi Dam was analyzed using the MAF-SSA-LSTM model. The prediction effect was visualized in Figure 17a,b. Meanwhile, the prediction results of different models are displayed in Figure 17c.

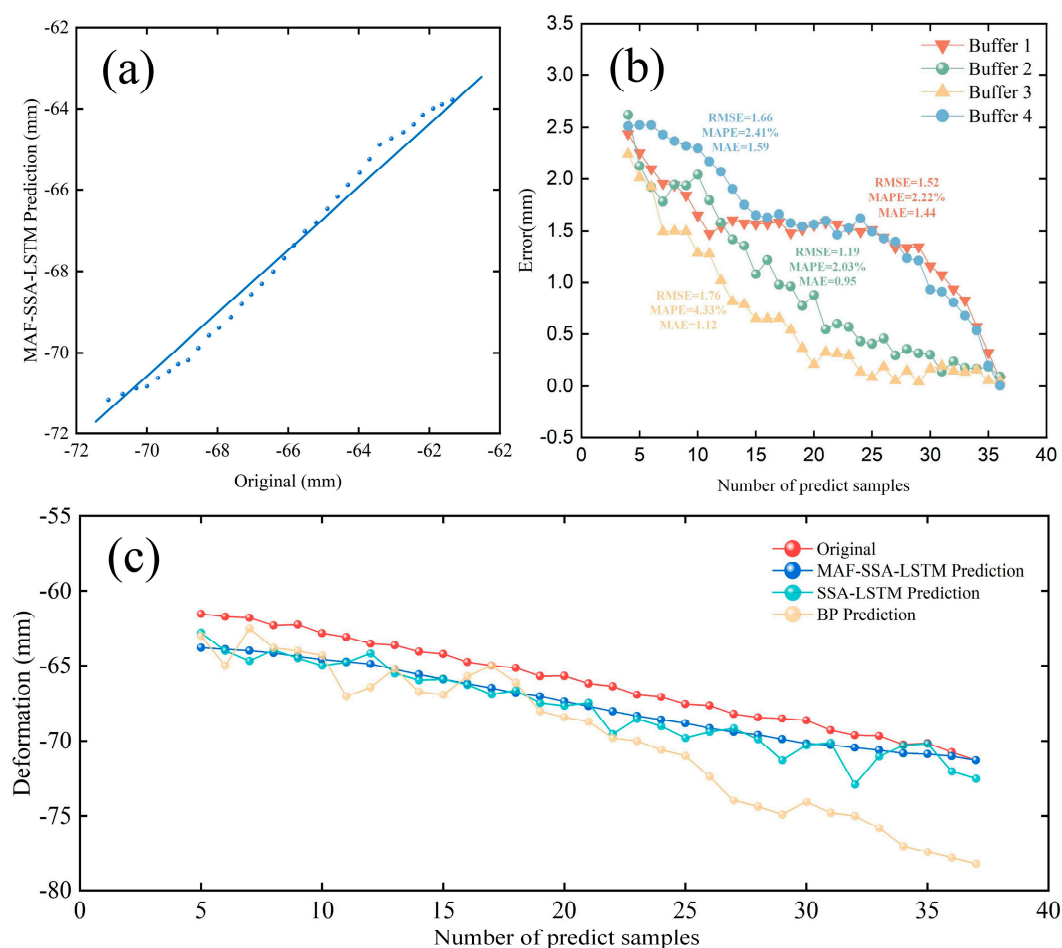


**Figure 17.** (a) Correlation between predicted value and original value of MAF-SSA-LSTM model; (b) prediction error curve of different buffers; (c) comparison of prediction results of three network models.

Figure 17a shows a scatter plot of the true and predicted deformation data as represented by the blue line. It is observed that the two are closely aligned and are roughly

on the same line with only slight fluctuations. There is a good correlation between the predicted value and the original value.

Figure 17b represents the prediction error curve of different buffers. The maximum prediction error is 2.61 mm. As the number of predicted samples increases, the prediction error gradually decreases, and the minimum prediction error is 0.07 mm. Meanwhile, because this study uses the dataset split ratio of 80% training and 20% test, each sample represents 12 days (satellite repetition time). Therefore, 33 samples were used for prediction. The forecast time is about 396 days. To further prove the accuracy of the results of the MAF-SSA-LSTM model, four buffers of the same size were selected at an equal distance in the middle of the dam. The deformation was predicted using the MAF-SSA-LSTM model. The prediction error values of different regions were calculated, and we obtained the error between the predicted deformation and the real deformation in the four regions. RMSE, MAE, and MAPE were calculated. The prediction error of multiple buffers showed that the prediction error was gradually decreasing with the end of the prediction. The accuracy evaluation values of each region are less than 3% of the total error. It has been proven that the model has good reliability and accuracy.

Figure 17c represents the prediction results of three network models. The Sparrow Search Algorithm Long Short-Term Memory (SSA-LSTM) model and the Error Back Propagation (BP) model are traditional models used for deformation prediction. Select the same dataset to compare the accuracy of the three models. The red line represents PS-InSAR monitoring results, and different color curves represent the prediction results of different models. It can be seen from the figure that the deformation prediction using the MAF-SSA-LSTM model has good reliability. Compared with the other two neural networks, RMSE decreased by 0.145 and 0.778. Compared with the SSA-LSTM model, the optimized network model has a trend closer to the real monitoring data in maintaining a low prediction error. Compared with the BP algorithm, the prediction error of the optimized network model is improved, and the prediction accuracy is significantly improved. The MAF-SSA-LSTM model shows great advantages. The results indicate that the MAF-SSA-LSTM model used in this study can approximate the trend of the PS-InSAR monitoring curve.

To intuitively analyze the prediction performance, three regression prediction metrics were selected to evaluate the performance of the MAF-SSA-LSTM model's prediction algorithm. These metrics include Root-Mean-Squared Error (RMSE), Mean Absolute Error (MAE), and Mean Absolute Percentage Error (MAPE) [51].

$$RMSE(y_i, \hat{y}) = \sqrt{\frac{1}{m} \sum_1^m (y_i - \hat{y})^2} \quad (9)$$

$$MAE(y_i, \hat{y}) = \frac{1}{m} \sum_1^m |y_i - \hat{y}| \quad (10)$$

$$MAPE(y_i, \hat{y}) = \frac{1}{m} \sum_1^m \frac{|y_i - \hat{y}|}{|y_i|} \quad (11)$$

where  $y_i$  is the smoothed true deformation data,  $\hat{y}$  is the predicted values, and  $m$  is the number of predicted data. The RMSE measures the accuracy of the model's predictions, the MAE provides an assessment of prediction errors, and the MAPE evaluates the model's overall accuracy. The smaller the calculated evaluation value, the better the prediction performance and the higher the prediction accuracy.

From Figure 17a,b, it can be observed that after comparing with InSAR deformation monitoring values, the results show that the MAF-SSA-LSTM model has an RMSE of 1.526 mm, MAE of 1.447 mm, maximum absolute error of 2.44 mm, and minimum absolute error of 0.07 mm. Additionally, Figure 17c shows that the predicted results are consistent with the deformation trend as monitored by the InSAR technique. This indicates that the MAF-SSA-LSTM model effectively predicts deformation. Furthermore, the MAPE of 2.22% shows the reliability of the MAF-SSA-LSTM model's prediction accuracy, further

demonstrating the feasibility of the model and providing accurate predictions for disaster warnings.

#### 5.4. Stability Analysis of Soil and Rockfill Dam

To further verify the monitoring results of PS-InSAR, the finite element analysis method is used to analyze the stress and seepage of Xiaolangdi soil and rockfill dam. The Xiaolangdi Reservoir Dam is divided into the main dam and an auxiliary dam. The main dam is located on the foundation of a deep overburden layer with an inner covering of a loam soil-inclined core rockfill dam. The maximum dam height is 160 m, the dam crest elevation is 281 m, the dam crest length is 1667 m, and the width is 15 m. The upstream slope ratio is 1:2.6 above the elevation of the main dam 185 m and 1:3.5 below. The downstream slope ratio is 1:1.75 above the elevation of 155 m and 1:2.5 below. The two-dimensional finite element analysis of the soil and rockfill dam is carried out from the static aspect by using the finite element analysis software. The values are taken according to the Duncan-Chang E-B model parameters and the material mechanics of Xiaolangdi soil and rockfill dam. The soil and rockfill dam model and dam material zoning are shown in Figure 18a, and the dam stress and seepage distribution are shown in Figure 18b,c.

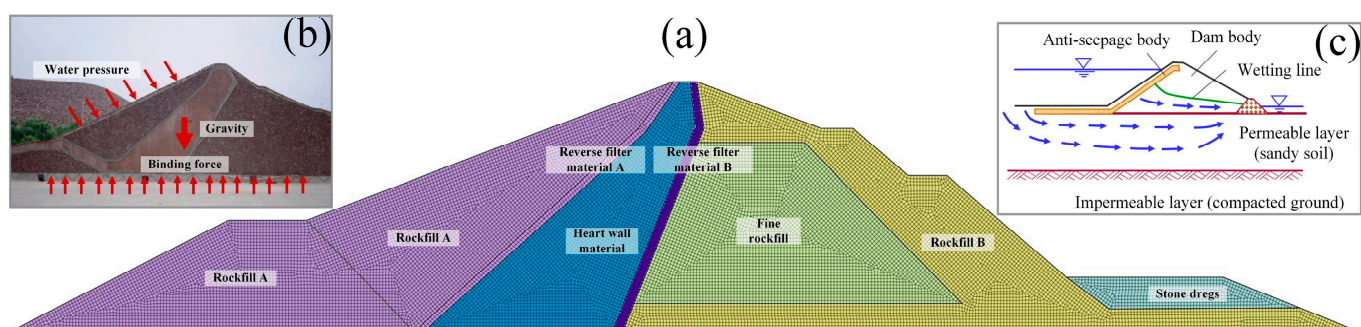


**Figure 18.** (a) Soil and rockfill dam model and dam material zoning; (b) force distribution diagram; (c) seepage distribution map.

##### 5.4.1. Seepage Stability Analysis

The nonlinear elastic incremental Duncan-Chang E-B model is used to determine the parameter values through a triaxial compression test. Different material mechanics values are determined according to different material zones. Different loads and boundary conditions are applied to calculate the seepage state of Xiaolangdi soil and rockfill dam and the deformation caused by the force on the dam body. The seepage steady-state analysis of soil and rockfill dam is carried out by using water levels at different heights, and the results are shown in Figure 19.

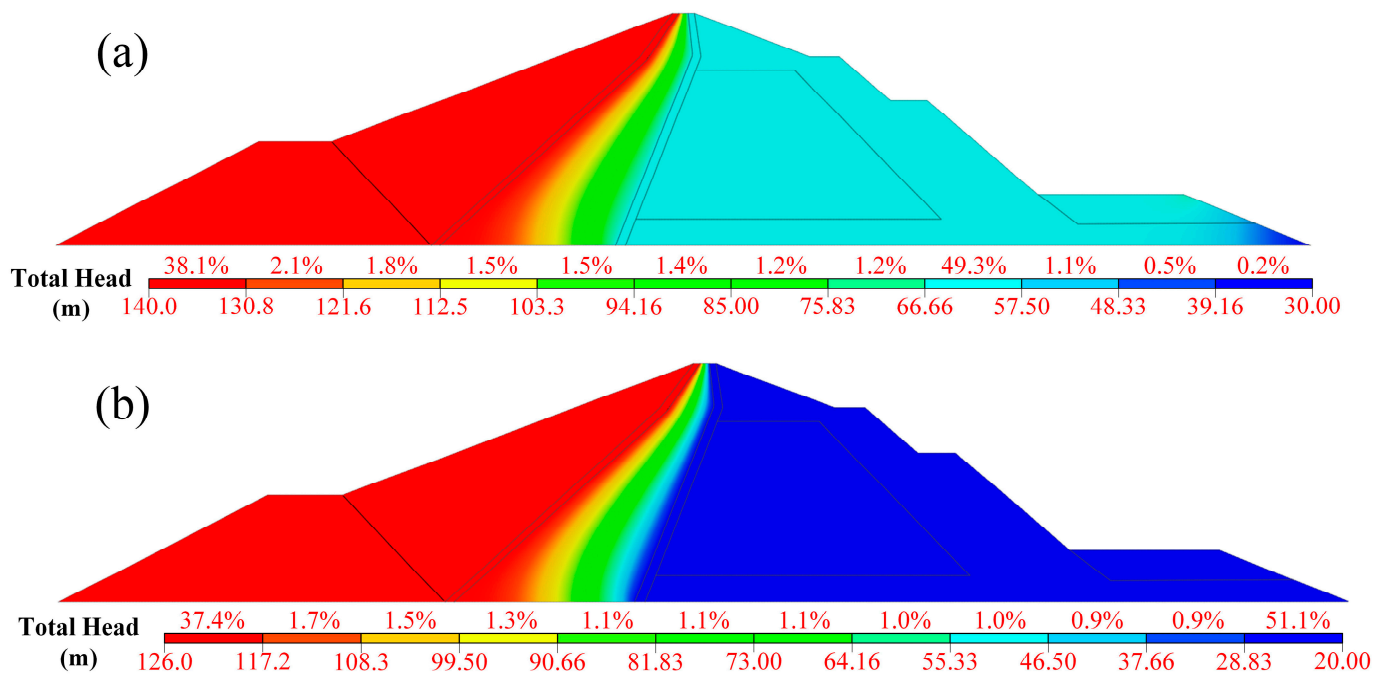


**Figure 19.** (a) Map of total head distribution in high water level dam body; (b) map of the total head distribution of the dam body at low water level (down 15 m compared with high water level).

It can be seen from the chart of total head distribution of soil and rockfill dam in Figure 19. Due to the impoundment of the upstream dam slope of the soil and rockfill dam, the water head distribution is the same, but it is uniformly distributed in the core wall area. In the downstream dam slope, due to the existence of downstream water storage, the water head at the slope toe is different from that in other areas. The core wall location is the main seepage area, and the low permeability of the core wall material makes it the main building to block the water infiltration. The pressure head formed at the upstream slope toe is the largest, and the pressure head formed at the downstream slope crest is the smallest. The total head is distributed from high to low, especially in the core wall area. This is due to the role of the core wall and impervious core, so the head pressure of the downstream dam slope is low. As can be seen from Figure 19b, the distribution of low water levels is roughly the same as that of high water levels. However, in the case of low water levels, the seepage of the dam body will be reduced compared with the high water levels. It can be seen that the core wall area of the soil and rockfill dam plays an important role in water infiltration and enhances the stability of the downstream dam slope. Under different water levels, the internal seepage trend of the dam body is consistent, and the core wall area plays a great role in the protection of the soil and rockfill dam. This is consistent with the conclusion drawn in Section 4, so the key monitoring of the core wall area should be strengthened.

#### 5.4.2. Stress Stability Analysis

Because the soil and rockfill dam is a water-holding structure that is submerged for an extended period, the dam body can experience deformation and damage due to the pressure of water and gravity, leading to dam instability. Therefore, the stability of the soil and rockfill dam during the impoundment period is analyzed. During the impounding period, when the water level in the reservoir reaches 260 m, the displacement maps of both horizontal and vertical components of the dam body are computed, as shown in Figure 20.

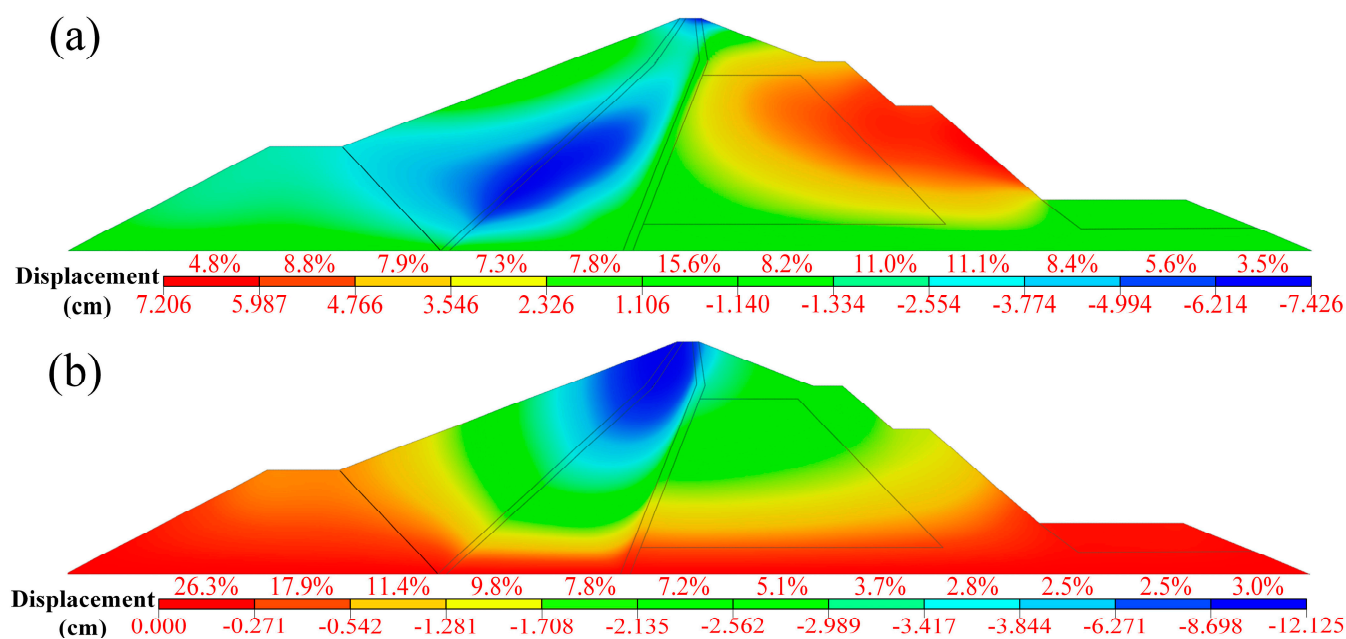


Figure 20. (a) Horizontal displacement map; (b) vertical displacement map.

During the impounding period, the maximum horizontal displacement of the soil and rockfill dam is  $-7.426$  cm, the maximum vertical displacement is  $-12.125$  cm, the maximum effective stress in the horizontal direction is  $89.879$   $\text{KN}/\text{m}^2$ , and the maximum effective stress in the vertical direction is  $35.272$   $\text{KN}/\text{m}^2$ . According to Figure 20a, in the horizontal direction, when the dam body is under the upstream water pressure, the displacement of the core wall is the largest, and it is found that the core wall plays an important role as a water-holding structure. According to Figure 20b, the displacement of the dam body from the dam crest to the dam bottom presents a “stepped” deformation state in the vertical direction. The model result is the same as the deformation state monitored by the InSAR technique. In addition, the horizontal stress generated during impoundment is greater than the vertical stress, which is because the water pressure generated within the upstream will be greater in the lateral pressure during impoundment. Under the influence of the gravity of the dam body, the compressive stress of the dam body from top to bottom decreases in turn. From the above conclusion, the horizontal displacement and vertical displacement are in line with the general deformation law of the dam and are consistent with the deformation trend of the dam body monitored by InSAR.

## 6. Conclusions

This study uses Sentinel-1A images and the PS-InSAR technique to monitor the deformation of large-scale soil and rockfill dams in Henan Province and focuses on analyzing the Xiaolangdi Reservoir soil and rockfill dam. The results show that most of the dam bodies of large-scale reservoirs experience deformation or lifting at different locations under long-term monitoring. Among the types of soil and rockfill dams, clay heart wall sand shell dams are relatively stable, while the dams of Baisha Reservoir, Baiguishan Reservoir, and Yanshan Reservoir, and surrounding areas show an overall deformation state, indicating that these reservoirs should be regarded as key concern areas.

Taking Xiaolangdi Reservoir as an example, it was found that the deformation rate of the soil and rockfill dam from the top to the bottom exhibited a stepped shape deformation pattern from 2017 to 2021. In addition, by choosing the deformation points of the key parts of the Xiaolangdi soil and rockfill dam, a deformation curve was drawn. The results showed that the upper part of the Xiaolangdi Reservoir soil and rockfill dam had sunk by about 80 mm in nearly 5 years, with a linear trend in the deformation curve. The middle part of the dam had sunk by around 40 mm, with a slower relative deformation

compared with the upper part and a slight oscillation. The lower part had sunk by about 20 mm and was always subject to large-scale oscillation. It was found that the middle part of the Xiaolangdi soil and rockfill dam had obvious deformation after analyzing the distribution of cross-section and longitudinal-section, and the longitudinal section analysis showed significant deformation at the top of the Xiaolangdi Reservoir soil and rockfill dam. Furthermore, the MAF-SSA-LSTM dam time series prediction model was established, and it was analyzed that the Xiaolangdi soil and rockfill dam would exhibit obvious deformation in about 2 years. The relationship between the water level and the deformation of Xiaolangdi Reservoir was discussed, and it was found that the high or low water level and rainfall amount have a certain influence on dam deformation. Therefore, after a long period of water level changes, the management department should conduct a check in key areas of the dam body and timely handle any safety hazards. The deformation monitoring of large-scale soil and rockfill dams illustrated that the application of the time series InSAR technique can survey the deformation of dams on a large scale, and with long-term monitoring results, the overall deformation pattern of soil and rockfill dams can be revealed. This indicates that the time series InSAR deformation monitoring method can provide reliable analysis and data support for disaster prevention and control of large-scale hydraulic structures.

In this study, only Sentinel-1A ascending orbit images were used for deformation monitoring of large-scale soil and rockfill dams in Henan Province. This can only obtain the deformation information in the LOS direction. In the future, ascending and descending orbit data can be used to invert the three-dimensional deformation information of soil and rockfill dams to obtain a more accurate deformation pattern. Additionally, due to confidentiality reasons, this study lacks contemporaneous leveling data for precise verification.

**Author Contributions:** Conceptualization, H.L.; methodology, M.Z.; software, B.Z.; validation, W.Z. (Wenfei Zhao); formal analysis, Y.W.; investigation, G.L.; resources, Z.B.; data curation, W.Z. (Wu Zhu); writing—original draft preparation, H.L.; writing—review and editing, M.Z. All authors have read and agreed to the published version of the manuscript.

**Funding:** This research was supported by the National Nature Science Foundation of China (grant No. 41901411), in part by the Henan Provincial Science and Technology Research Project (grant No. 212102310052), in part by the Training Plan for Young Backbone Teachers of Colleges and Universities in Henan Province (grant No. 2021GGJS073), in part by the Open Foundation of Key Laboratory of Ecological Environment Protection of Space Information Application of Henan (grant No. 22-FW-07-0107), in part by the Major Science and Technology Special Projects in Henan Province (grant No. 201300311400), and in part by the Joint Fund of Collaborative Innovation Center of Geo-Information Technology for Smart Central Plains, Henan Province and Key Laboratory of Spatiotemporal Perception and Intelligent Processing, Ministry of Natural Resources (grant No. 211103), Key scientific research projects of colleges and universities in Henan Province (grant No. 21A420005).

**Data Availability Statement:** The water level dataset is provided by the Yellow River Conservancy Commission of the Ministry of Water Resources (<http://www.yrcc.gov.cn/>, accessed on 31 December 2022). The rainfall data is provided by the Henan Provincial Hydrology and Water Resources Measurement and Reporting Center (<http://www.hnssw.com.cn/>, accessed on 31 December 2022).

**Acknowledgments:** Thanks for the valuable feedback provided by the editor and expert, and we thank the European Space Agency (ESA) and European Commission (EC) for their efforts in developing and distributing the remotely sensed SAR data.

**Conflicts of Interest:** The authors declare no conflict of interest.

## References

1. National Bureau of Statistics. *2020 China Statistical Yearbook*; China Statistics Press: Beijing, China, 2021.
2. Liu, W.; Liu, H.; Song, Z.; Hu, Q. Discussion on Iterative Construction Strategy and Application of Domestic Inland Water in SAR Satellite Constellation. *J. North China Univ. Water Resour. Electr. Power Nat. Sci. Ed.* **2022**, *43*, 1–10.
3. Sheng, J.; Li, H.; Sheng, T. Statistical analysis of dam failure and its loss of life in China. *Hydro-Sci. Eng.* **2023**, *1*, 1–15.

4. Liu, H.; Yue, J.; Liu, W.; Huang, Q.; Li, G.; Liu, M. Multi-baseline phase unwrapping with robust branch and bound pure integer programming algorithm. *Opt. Lasers Eng.* **2023**, *161*, 107352. [[CrossRef](#)]
5. Liu, H. Research on Antennas Design and Three-Dimensional Imaging Techniques for MIMO Sparse Array SAR. Ph.D. Thesis, Information Engineering University, Zhenzhou, China, 2017.
6. Jänichen, J.; Schmallius, C.; Baade, J.; Last, K.; Bettzieche, V.; Dubois, C. Monitoring of Radial Deformations of a Gravity Dam Using Sentinel-1 Persistent Scatterer Interferometry. *Remote Sens.* **2022**, *14*, 1112. [[CrossRef](#)]
7. Ruiz-Armenteros, A.; Lazecky, M.; Hlaváčová, I.; Bakoň, M.; Delgado, J.; Sousa, J.; Lamas-Fernández, F.; Marchamalo, M.; Caro-Cuenca, M.; Papco, J.; et al. Deformation monitoring of dam infrastructures via spaceborne MT-InSAR. The case of La Viñuela (Málaga, Southern Spain). *Procedia Comput. Sci.* **2018**, *138*, 346–353. [[CrossRef](#)]
8. Othman, A.; Al-Maamar, A.; Al-Manmi, D.; Liesenberg, V.; Hasan, S.; Al-Saady, Y.; Shihab, A.; Khwedim, K. Application of DInSAR-PSI technology for deformation monitoring of the Mosul dam, Iraq. *Remote Sens.* **2019**, *11*, 2632. [[CrossRef](#)]
9. Zhang, Q.; Zhao, C.; Ding, X.; Chen, Y.; Wang, L.; Huang, G.; Yang, C.; Ding, X.; Jing, M. Research on recent characteristics of spatio-temporal evolution and mechanism of Xi'an land subsidence and ground fissure by using GPS and InSAR techniques. *Chin. J. Geophys.* **2009**, *52*, 1214–1222.
10. Liu, Q.; Zhang, Y.; Deng, M.; Wu, H.; Kang, Y. Time series prediction method of large-scale surface subsidence based on deep learning. *Acta Geod. Et Cartogr. Sin.* **2021**, *50*, 396–404.
11. Liu, H.; Xu, Q.; Jin, G.; Lou, L. Urban Buildings MIMO Downward-Looking Array SAR 3D Simulation Under Non-ideal Trajectory. *Geomat. Inf. Sci. Wuhan Univ.* **2019**, *44*, 413–421+442.
12. Aslan, G.; Fomelis, M.; Raucoules, D.; Michele, M.; Bernardie, S.; Cakir, Z. Landslide Mapping and Monitoring Using Persistent Scatterer Interferometry (PSI) Technique in the French Alps. *Remote Sens.* **2020**, *12*, 1305. [[CrossRef](#)]
13. Nefros, C.; Alatza, S.; Loupasakis, C.; Kontoes, C. Persistent Scatterer Interferometry (PSI) Technique for the Identification and Monitoring of Critical Landslide Areas in a Regional and Mountainous Road Network. *Remote Sens.* **2023**, *15*, 1550. [[CrossRef](#)]
14. Liao, M.; Tang, Q.; Wang, T.; Timo, B.; Zhang, L. Application of High Resolution SAR Data in Landslide Monitoring in Three Gorges Reservoir Area. *Sci. China Earth Sci.* **2012**, *42*, 217–229.
15. Wu, H.; Zhang, Y.; Zhong, W. Monitoring Mine Subsidence with Time-Series SAR Interferometry. *Adv. Mater. Res.* **2012**, *524–527*, 618–621. [[CrossRef](#)]
16. Ng, H.; Ge, L.; Yan, Y.; Li, X.; Chang, H.; Zhang, K.; Rizos, C. Mapping accumulated mine subsidence using small stack of SAR differential interferograms in the Southern coalfield of New South Wales, Australia. *Eng. Geol.* **2010**, *115*, 1–15. [[CrossRef](#)]
17. Zhou, L.; Zhang, D.; Jie, W.; Huang, Z.; Pan, D. Mapping Land Subsidence Related to Underground Coal Fires in the Wuda Coalfield (Northern China) Using a Small Stack of ALOS PALSAR Differential Interferograms. *Remote Sens.* **2013**, *5*, 1152–1176. [[CrossRef](#)]
18. Liu, H.; Yue, J.; Huang, Q.; Li, G.; Liu, M. A Novel Branch and Bound Pure Integer Programming Phase Unwrapping Algorithm for Dual-Baseline InSAR. *Front. Environ. Sci.* **2022**, *10*, 890343. [[CrossRef](#)]
19. Xu, X.; Sandwell, D.; Smith-Konter, B. Coseismic displacements and surface fractures from Sentinel-1 InSAR: 2019 Ridgecrest earthquakes. *Sesmol. Res. Lett.* **2020**, *91*, 1979–1985. [[CrossRef](#)]
20. Ji, Y.; Sumantyo, J.; Chua, M.; Waqar, M. Earthquake/tsunami damage level mapping of urban areas using full polarimetric SAR data. *IEEE J. Sel. Top. Appl. Earth Obs. Remote. Sens.* **2018**, *11*, 2296–2309. [[CrossRef](#)]
21. Liu, J.; Hu, J.; Li, Z.; Ma, Z.; Shi, J.; Xu, W.; Sun, Q. Three-dimensional surface displacements of the 8 January 2022 Mw6.7 Menyuan earthquake, China from Sentinel-1 and ALOS-2 SAR observations. *Remote Sens.* **2022**, *14*, 1404. [[CrossRef](#)]
22. Necsoiu, M.; Onaca, A.; Wigginton, S.; Urdea, P. Rock glacier dynamics in Southern Carpathian Mountains from high-resolution optical and multi-temporal SAR satellite imagery. *Remote Sens. Environ.* **2016**, *177*, 21–36. [[CrossRef](#)]
23. Mohammadimanes, F.; Salehi, B.; Mahdianpari, M.; English, J.; Chamberland, J.; Alasset, P. Monitoring surface changes in discontinuous permafrost terrain using small baseline SAR interferometry, object-based classification, and geological features: A case study from Mayo, Yukon Territory, Canada. *Gisci. Remote Sens.* **2019**, *56*, 485–510. [[CrossRef](#)]
24. Ye, Y.; Xiaolei, L.; Xikai, F.; Feiyang, X. Application of spaceborne interferometric synthetic aperture radar to geohazard monitoring. *J. Radars* **2020**, *9*, 73–85.
25. Cigna, F.; Osmanoğlu, B.; Cabral-Cano, E.; Dixon, T.; Ávila-Olivera, J.; Garduño-Monroy, V.; DeMets, C.; Wdowinski, S. Monitoring land subsidence and its induced geological hazard with Synthetic Aperture Radar Interferometry: A case study in Morelia, Mexico. *Remote Sens. Environ.* **2012**, *117*, 146–161. [[CrossRef](#)]
26. Kussul, N.; Shelestov, A.; Skakun, S. Flood monitoring from SAR data. In *Use of Satellite and In-Situ Data to Improve Sustainability*; Springer: Dordrecht, The Netherlands, 2011; Volume 97, pp. 19–29.
27. Mura, J.; Gama, F.; Paradella, W.; Negrão, P.; Carneiro, S.; De Oliveira, C.; Brandão, W. Monitoring the vulnerability of the dam and dikes in Germano iron mining area after the collapse of the tailings dam of Fundão (Mariana-MG, Brazil) using DInSAR techniques with TerraSAR-X data. *Remote Sens.* **2018**, *10*, 1507. [[CrossRef](#)]
28. Scaioni, M.; Marsella, M.; Crosetto, M.; Tornatore, V.; Wang, J. Geodetic and remote-sensing sensors for dam deformation monitoring. *Sensors* **2018**, *18*, 3682. [[CrossRef](#)]
29. Liu, G.; Guo, H.; Perski, Z.; Fan, J.; Bai, S.; Yan, S.; Song, R. Monitoring the slope movement of the Shuping landslide in the Three Gorges Reservoir of China, using X-band time series SAR interferometry. *Adv. Space Res.* **2016**, *57*, 2487–2495. [[CrossRef](#)]

30. Perissin, D.; Wang, T. Time-series InSAR applications over urban areas in China. *IEEE J. Sel. Top. Appl. Earth Obs. Remote. Sens.* **2010**, *4*, 92–100. [[CrossRef](#)]
31. Qiu, Z.; Jiao, M.; Jiang, T.; Zhou, L. Dam structure deformation monitoring by GB-InSAR approach. *IEEE Access* **2020**, *8*, 123287–123296. [[CrossRef](#)]
32. Sousa, J.; Ruiz, A.; Bakoň, M.; Lazecky, M.; Hlaváčová, I.; Patricio, G.; Delgado, J.; Perissin, D. Potential of C-band SAR interferometry for dam monitoring. *Procedia Comput. Sci.* **2016**, *100*, 1103–1114. [[CrossRef](#)]
33. Voege, M.; Frauenfelder, R.; Larsen, Y. Displacement monitoring at Svartevatn dam with interferometric SAR. In Proceedings of the 2012 IEEE International Geoscience and Remote Sensing Symposium, Munich, Germany, 22–27 July 2012; pp. 3895–3898.
34. Wang, J.; Zhang, Q.; Gou, T.; Mo, J.; Wang, Z.; Gao, M. Spatial-temporal changes of urban areas and terrestrial carbon storage in the Three Gorges Reservoir in China. *Ecol. Indic.* **2018**, *95*, 343–352. [[CrossRef](#)]
35. Li, T.; Motagh, M.; Wang, M.; Zhang, W.; Gong, C.; Xiong, X.; He, J.; Chen, L.; Liu, J. Earth and rock-filled dam monitoring by high-resolution X-band interferometry: Gongming dam case study. *Remote Sens.* **2019**, *11*, 246. [[CrossRef](#)]
36. Liu, H.; Zhao, W.; Qin, Z.; Wang, T.; Li, G.; Zhu, M. Time-Series InSAR Deformation Monitoring of High Fill Characteristic Canal of South-North Water Diversion Project in China. *Appl. Sci.* **2023**, *13*, 6415. [[CrossRef](#)]
37. Lee, S.; Lee, K.; Yoon, H. Using artificial neural network models for groundwater level forecasting and assessment of the relative impacts of influencing factors. *Hydrogeol. J.* **2019**, *27*, 567–579. [[CrossRef](#)]
38. Kumar, H.; Syed, T.; Amelung, F.; Agrawal, R.; Venkatesh, A. Space-time evolution of land subsidence in the National Capital Region of India using ALOS-1 and Sentinel-1 SAR data: Evidence for groundwater overexploitation. *J. Hydrol.* **2022**, *605*, 127329. [[CrossRef](#)]
39. Sharaky, A.; Elewa, H.; Kasem, A. Impact of the Grand Ethiopian Renaissance Dam (GERD) on Gezira Groundwater, Sudan. In *Grand Ethiopian Renaissance Dam Versus Aswan High Dam*; Springer International Publishing AG: Cham, Germany, 2019; Volume 79, pp. 519–557.
40. Aswathi, J.; Binojkumar, R.; Oommen, T.; Bouali, E.; Sajinkumar, K. InSAR as a tool for monitoring hydropower projects: A review. *Energy Geosci.* **2022**, *3*, 160–171. [[CrossRef](#)]
41. Wang, Q.; Huang, Q.; He, N.; He, B.; Wang, Z.; Wang, Y. Displacement monitoring of upper Atbara dam based on time series InSAR. *Surv. Rev.* **2020**, *52*, 485–496. [[CrossRef](#)]
42. Yu, H.; Jiang, X.; Zhang, Q.; Cao, L. Analysis of Arching Effect of Core Wall of Xiaolangdi Dam. *Yellow River* **2017**, *39*, 135–137.
43. Zhang, W.; Zhu, W.; Tian, X.; Zhang, Q.; Wang, C. Improved DEM Reconstruction Method Based on Multibaseline InSAR. *IEEE Geosci. Remote. Sens. Lett.* **2021**, *99*, 1–5. [[CrossRef](#)]
44. Ferretti, A.; Prati, C.; Rocca, F. Nonlinear subsidence rate estimation using permanent scatterers in differential SAR interferometry. *IEEE Trans. Geosci. Remote Sens.* **2000**, *38*, 2202–2212. [[CrossRef](#)]
45. Fiorentini, N.; Maboudi, M.; Leandri, P.; Losa, M. Can Machine Learning and PS-InSAR Reliably Stand in for Road Profilometric Surveys? *Sensors* **2021**, *21*, 3377. [[CrossRef](#)]
46. Evers, M.; Kyriou, A.; Thiele, A.; Hammer, H.; Nikolakopoulos, K.; Schulz, K. How to set up a dam monitoring system with PSInSAR and GPS. *SPIE Remote Sens.* **2020**, 11534, 115340L.
47. Liu, H.; Zhou, B.; Bai, Z.; Zhao, W.; Zhu, M.; Zheng, K.; Yang, S.; Li, G. Applicability Assessment of Multi-Source DEM-Assisted InSAR Deformation Monitoring Considering Two Topographical Features. *Land* **2023**, *12*, 1284. [[CrossRef](#)]
48. Xue, J.; Shen, B. A novel swarm intelligence optimization approach: Sparrow search algorithm. *Syst. Sci. Control Eng.* **2020**, *8*, 22–34. [[CrossRef](#)]
49. SL274-2020; Design Code for Rolled Earth Rock Fill Dams. *Ministry of Water Resources of the People's Republic of China*; China Water Resources and Hydropower Press: Beijing, China, 2020.
50. He, Z.; Yu, H.; Xie, S.; Yu, L.; Chen, L. Deformation monitoring of Xiaolangdi dam based on SBAS-InSAR technology. *Sci. Surv. Mapp.* **2022**, *47*, 66–72+82.
51. Chai, T.; Draxler, R. Root mean square error (RMSE) or mean absolute error (MAE)?—Arguments against avoiding RMSE in the literature. *Geosci. Model Dev.* **2014**, *7*, 1247–1250. [[CrossRef](#)]

**Disclaimer/Publisher's Note:** The statements, opinions and data contained in all publications are solely those of the individual author(s) and contributor(s) and not of MDPI and/or the editor(s). MDPI and/or the editor(s) disclaim responsibility for any injury to people or property resulting from any ideas, methods, instructions or products referred to in the content.